

## Viscously Stirring Particle Disks into Lorentzians and Gaussians to Infer Dynamical and Collisional Masses (ARKS XIII)

EUGENE CHIANG,<sup>1,2</sup> TIM D. PEARCE,<sup>3</sup> MARIJA R. JANKOVIC,<sup>4</sup> ALEXANDER JEFFREY BACKUES,<sup>5,6</sup> YINUO HAN,<sup>7</sup>  
ALEXANDER V. KRIVOV,<sup>8</sup> MARGARET PAN,<sup>9</sup> BRIANNA ZAWADZKI,<sup>10</sup> A. MEREDITH HUGHES,<sup>10</sup>  
KRISH PRAKASH JHURANI,<sup>1,5</sup> JOSHUA B. LOVELL,<sup>9</sup> SEBASTIÁN MARINO,<sup>11</sup> ANTRANIK A. SEFILIAN,<sup>12</sup> DAVID J. WILNER,<sup>9</sup>  
MARK C. WYATT,<sup>13</sup> SEBASTIÁN PÉREZ,<sup>14, 15, 16</sup> PÉTER ÁBRAHÁM,<sup>17, 18</sup> ÁGNES KÓSPÁL,<sup>17</sup> AND PATRICIA LUPPE<sup>19</sup>

<sup>1</sup>*Department of Astronomy, University of California, Berkeley, 501 Campbell Hall, Berkeley CA 94720-3411, USA*

<sup>2</sup>*Department of Earth and Planetary Science, University of California, Berkeley, 307 McCone Hall, Berkeley, CA 94720-4767, USA*

<sup>3</sup>*Department of Physics, University of Warwick, Gibbet Hill Road, Coventry CV4 7AL, UK*

<sup>4</sup>*Institute of Physics Belgrade, University of Belgrade, Pregrevica 118, 11080 Belgrade, Serbia*

<sup>5</sup>*Department of Physics, University of California, Berkeley, 366 Physics North MC 7300, Berkeley, CA 94720-7300, USA*

<sup>6</sup>*EECS Computer Science Division, University of California, Berkeley, 387 Soda Hall, Berkeley, CA 94720-1776, USA*

<sup>7</sup>*Division of Geological and Planetary Sciences, California Institute of Technology, 1200 E. California Blvd., Pasadena, CA 91125, USA*

<sup>8</sup>*Astrophysikalisches Institut und Universitätssternwarte, Friedrich-Schiller-Universität Jena, Schillergäßchen 2-3, 07745 Jena, Germany*

<sup>9</sup>*Center for Astrophysics | Harvard & Smithsonian, 60 Garden Street, Cambridge, MA 02138, USA*

<sup>10</sup>*Department of Astronomy, Van Vleck Observatory, Wesleyan University, 96 Foss Hill Dr., Middletown, CT 06459, USA*

<sup>11</sup>*Department of Physics and Astronomy, University of Exeter, Stocker Road, Exeter EX4 4QL, UK*

<sup>12</sup>*Department of Astronomy and Steward Observatory, University of Arizona, Tucson, AZ 85721, USA*

<sup>13</sup>*Institute of Astronomy, University of Cambridge, Madingley Road, Cambridge, CB3 0HA, UK*

<sup>14</sup>*Departamento de Física, Universidad de Santiago de Chile. Avenida Ecuador 3493, Estación Central, Santiago, Chile*

<sup>15</sup>*Millennium Nucleus on Young Exoplanets and their Moons (YEMS), Chile*

<sup>16</sup>*Center for Interdisciplinary Research in Astrophysics and Space Exploration (CIRAS), Universidad de Santiago de Chile, Chile*

<sup>17</sup>*Konkoly Observatory, HUN-REN Research Centre for Astronomy and Earth Sciences, MTA Centre of Excellence, Konkoly-Thege Miklós út 15-17, 1121 Budapest, Hungary*

<sup>18</sup>*Department of Astrophysics, University of Vienna, Türkenschanzstrasse 17, 1180 Vienna, Austria*

<sup>19</sup>*School of Physics, Trinity College Dublin, the University of Dublin, College Green, Dublin 2, Ireland*

Submitted to AAS Journals

### ABSTRACT

Disks (Keplerian or otherwise, particulate or fluid) are often assumed to have densities that drop off vertically as Gaussians. Recent mm-wave imaging of circumstellar debris disks contradicts this assumption, revealing vertical profiles in dust that resemble Lorentzians. As part of the ARKS ALMA Large Program, we calculate how Lorentzians and Gaussians define an evolutionary sequence for disks of gravitationally scattering (viscously stirring) particles. When orbits are crossing and eccentricities  $e \gg$  inclinations  $i$ , each scattering changes a particle's inclination by  $\pm \Delta i \propto i$ . A random walk with fixed steps in  $\Delta i/i = \Delta \ln i$  produces a log normal  $i$  distribution, whose thick tail at large  $i$  leads to Lorentzian tails in density. This result holds independent of the origin of the large eccentricities; what matters is that relative motions parallel to the disk midplane are faster than perpendicular motions. After enough scatterings,  $i$  comes into equipartition with  $e$ ,  $\Delta i$  stops exponentiating, and the vertical density relaxes to a Gaussian. We estimate the numbers and masses of perturbers needed to stir themselves and observable dust grains in Lorentzian and Gaussian debris disks imaged by ARKS. The big bodies may be sufficiently few in number as to be collisionless, in which case their masses range from the Moon to several Earths. But if Pluto-sized or smaller, the big body stirrers may be so numerous and collide so frequently that they can source the collisional cascades that produce observable dust.

Corresponding author: E. Chiang

[echiang@astro.berkeley.edu](mailto:echiang@astro.berkeley.edu)

*Keywords:* debris disks, circumstellar disks, planetesimals, planetary dynamics, stellar dynamics, asteroid dynamics, galaxy dynamics, celestial mechanics, close encounters

## 1. INTRODUCTION

Astrophysical disks, particulate or fluid, form from objects that conserve their angular momentum and dissipate their energy, specifically their vertical kinetic energy (the energy in motions parallel to the angular momentum vector). A disk whose vertical kinetic energy damps to zero would have zero vertical thickness. In reality disks have non-zero thicknesses determined by processes that increase their vertical energy (e.g. accretional/turbulent heating; irradiation; viscous stirring) and decrease it (e.g. radiative loss; inelastic collisions between particles; dynamical friction cooling).

Disks (Keplerian and otherwise) are commonly assumed to have vertical density profiles that fall off as Gaussians with height above the midplane. Gaussian profiles characterize vertically isothermal gas disks (e.g. Frank et al. 2002), and disks of solid particles whose mutual interactions (via collisions or gravitational scatterings) establish energy equipartition between random (epicyclic) motions parallel and perpendicular to the midplane (e.g. Ida & Makino 1992). Gaussians abound in nature, a consequence of the central limit theorem and statistical equilibrium.

Surprisingly, Zawadzki et al. (2026, ARKS III) found that many of the brightest and youngest (10–1000 Myr old) debris disks in the mm-wave continuum exhibit vertical profiles with thick non-Gaussian tails. They made their observations as part of the ALMA survey to Resolve exoKuiper belt Substructures (ARKS; Marino et al. 2026, ARKS I) in circumstellar debris disks composed of optically thin dust. Debris disks are analogues of our Solar System’s Kuiper belt, and ARKS is an ALMA (Atacama Large Millimeter Array) Large Program designed to image the brightest disks in the thermal continuum (0.8–1.4 mm wavelength) and  $^{12}\text{CO}$  and  $^{13}\text{CO}$  ( $J=3-2$ ) at angular resolutions fine enough to resolve their heights and widths. When fitting the mm continuum visibilities of highly inclined disks, ARKS III found that Lorentzian vertical density profiles, and in one case a double Gaussian profile, were preferred with high formal confidence over single Gaussians in 10 out of 13 disks. They employed parameterized three-dimensional disk models presumed capable of disentangling vertical from radial structures. Ahmic et al. (2009), Matrà et al. (2019), and Han et al. (2026a) also reported vertical profiles broader than single Gaussians for the beta Pictoris debris disk.

The present paper, part of the ARKS series, seeks to understand the physical origin of vertical profiles that taper off more slowly than Gaussians. Non-Gaussian profiles were obtained in prior theoretical work by Sefilian et al. (2025) who examined secular vertical forcing/warping of a radially extended disk by a planet, accounting for the secular self-gravitational potential of the disk. Here, starting from first principles, we consider the non-secular and radially local problem. We study how “small bodies” (the collisional progenitors of the presumed mm-sized particles responsible for the ALMA emission) are gravitationally stirred by one or more “big bodies” on crossing orbits, stochastically on close encounter (synodic) timescales. We will see how such “viscous stirring” produces broad Lorentzian vertical profiles within a narrow disk annulus, and how Lorentzians and Gaussians bracket an evolutionary continuum. The dynamics is simple, local, and does not require warping or varying disk aspect ratios with radius.

Throughout this paper, “Lorentzian” really means “Lorentzian-like”, as vertical profiles must eventually deviate from strict Lorentzians far above the midplane. Our work does not rigorously prove a connection with Lorentzians; we only show that, under certain physical conditions, Lorentzians offer superior fits to numerically computed profiles, as compared to Gaussians. The same is true for the ALMA observations — for certain disks, the data prefer Lorentzians over Gaussians, but do not rule out other functional forms. We will usually drop the modifier “-like” for convenience.

### 1.1. *Origin of Rayleigh inclination distribution and Gaussian vertical distribution*

To lay the groundwork for our analysis, recall how Gaussian vertical profiles arise in a disk of particles that are stochastically perturbed. Imparting random impulses to a particle’s vertical velocity causes its angular momentum vector to random walk. The unit angular momentum vector random walks in 2D on the surface of the unit sphere; both the orbital inclination  $i$  of the particle and its longitude of ascending node  $\Omega$  change randomly with every “kick” in vertical velocity.

Consider an ensemble of particles that start with zero inclination, and have each particle take randomly directed steps in the 2D space  $(p, q) = (i \cos \Omega, i \sin \Omega)$ , with each step  $(\Delta p, \Delta q)$  of fixed length  $|\Delta i| = \sqrt{(\Delta p)^2 + (\Delta q)^2}$ . The assumption of a strictly fixed length is made for simplicity and is not necessary for

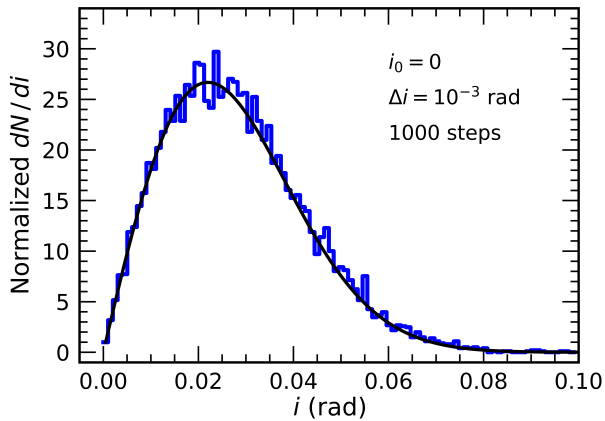


**Figure 1.** Fixed-length, randomly directed steps in  $(p, q) \equiv (i \cos \Omega, i \sin \Omega)$  space, starting from the origin  $i_0 = 0$ , give rise to a Rayleigh distribution  $\propto i \exp[-i^2/(2\sigma_i^2)]$ . Here 10000 particles each take 1000 random-walk steps of fixed length  $\Delta i = \sqrt{(\Delta p)^2 + (\Delta q)^2} = 10^{-3}$  rad (normalized data in blue, best-fit Rayleigh distribution with  $\sigma_i = 0.022$  in black).

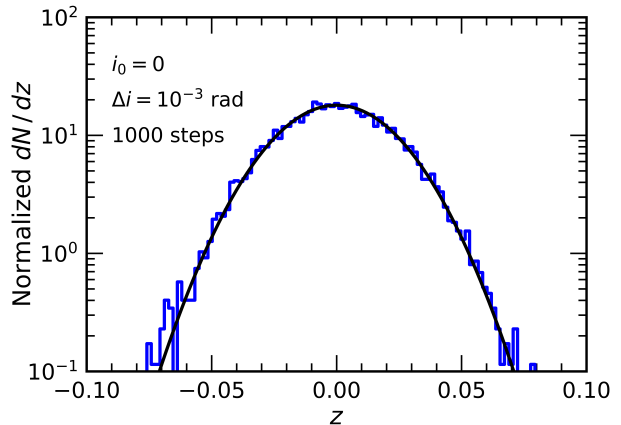
deriving a Gaussian profile;  $|\Delta i|$  can be drawn from any probability distribution, as long as it is of finite variance.

Figure 1 shows the inclination distribution  $dN/di$  of 10000 particles after they have taken  $S = 1000$  random-walk steps, each of length  $|\Delta i| = 10^{-3}$  rad. The inclination distribution conforms to a Rayleigh distribution  $\propto i \exp[-i^2/(2\sigma_i^2)]$  with  $\sigma_i \sim \sqrt{S}|\Delta i|$ . The Rayleigh distribution is what the central limit theorem predicts for a random walk on the surface of a sphere: the Rayleigh distribution is the product of a Gaussian and  $i$  (technically  $\sin i$ ), with the latter factor reflecting the available phase-space area near the polar cap of the unit sphere at small  $i$ .

Now convert each particle’s  $i$  to a height above the midplane  $z = a \sin i \sin u$ , assuming for simplicity zero eccentricity, semimajor axis  $a = 1$  (arbitrary units), and  $u$  (a particle’s angle from the ascending node, a.k.a. the argument of latitude) drawn randomly from a uniform variate  $[0, 2\pi)$ . The resultant vertical density profile  $dN/dz$ , computed by Monte Carlo sampling, is shown in Figure 2. It is a Gaussian with  $\sigma_z \sim a\sigma_i$ . The same result is obtained analytically by [Matrà et al. \(2019\)](#) by evaluating the sky-projection integral.

### 1.2. Plan of this paper

In the remainder of this paper we will see how the dynamics of viscous stirring can lead to a Lorentzian vertical profile as well as a Gaussian. The underlying idea is simple: the random-walk steps  $|\Delta i|$  are not necessarily of fixed length, but can grow in proportion to  $i$ . This exponentiation of the step size leads to broad



**Figure 2.** A Rayleigh distribution for  $dN/di$  leads to a Gaussian distribution for the vertical density profile  $dN/dz$ . Here the 10000  $i$ ’s from Fig. 1 are converted to vertical height  $z = a \sin i \sin u$ , where  $a = 1$  and  $u$  is drawn randomly as a uniform variate from 0 to  $2\pi$ , to generate  $dN/dz$  (normalized data in blue, best-fit Gaussian with  $\sigma_z = 0.022$  in black).

non-Gaussian tails. Section 2 details our semi-analytic (often order-of-magnitude) reasoning. Section 3 explores viscous stirring numerically with an  $N$ -body integrator. Section 4 applies our theory to Gaussian and Lorentzian disks from [ARKS III](#) to estimate how much mass they contain in big body stirrers. The results in Section 4 complement and are informed by a parallel [ARKS](#) paper by [Jankovic et al. \(2026, ARKS XII\)](#). Section 5 summarizes and provides an outlook.

## 2. THEORY OF VERTICAL STIRRING

We study how small bodies (test particles) are gravitationally stirred by big bodies, focussing on their vertical dynamics. We work in the dispersion-dominated regime where small and big bodies cross orbits, and consider both equipartition conditions when eccentricities are comparable to inclinations (rms eccentricity =  $2 \times$  rms inclination; e.g. [Ida & Makino 1992](#)), and out-of-equipartition (anisotropic) conditions when inclinations  $\ll$  eccentricities. Much of our reasoning in this section may be extended to the non-crossing, a.k.a. shear-dominated case, as discussed in [Appendix A](#); the shear-dominated case is less important than the dispersion-dominated case for real-life debris disks, whose present-day properties are inconsistent with shear-dominated self-stirring ([Jankovic et al. 2026](#)).

Also for simplicity in this section, we take big bodies to be on circular orbits in the reference plane. Many of our findings will still apply when big bodies are on eccentric orbits. What matters are the relative

motions between big and small bodies in and out of the reference plane, i.e. horizontal vs. vertical relative velocities. Vertical relative velocities depend on mutual inclinations  $i$ . Horizontal relative motions depend on “mutual” eccentricities — horizontal velocities can be large because small body eccentricities are large, or because big body eccentricities are large, or both. Thus the eccentricity  $e$  below, though formally referring to the small bodies, may be reinterpreted to include the eccentricities of both big and small bodies — roughly as their quadrature sum, assuming orbit orientations are uncorrelated. We will relax the assumption of zero big body eccentricity later.

### 2.1. How inclination changes in an encounter

After a small body undergoes a close encounter with a big body, their mutual inclination, assuming it is not initially zero, increases or decreases. The small body’s inclination  $i$  (relative to a reference plane which we take to coincide with the big body’s orbit plane) changes with time according to Gauss’s perturbation equation (e.g. Murray & Dermott 1999, equation 2.157):

$$\frac{di}{dt} = \frac{rN \cos(\omega + f)}{\ell} \quad (1)$$

where  $r$  is the radial distance of the small body from the central mass  $m_*$ ,  $\omega$  the argument of periaapse,  $f$  the true anomaly,  $\ell = \sqrt{Gm_*a(1 - e^2)}$  the specific angular momentum,  $a$  the semimajor axis,  $e$  the eccentricity,  $G$  the gravitational constant, and  $N$  the perturbing acceleration felt by the test particle normal to its own orbit. As Murray & Dermott (1999) state,  $rN \cos(\omega + f)$  is the component of the perturbing torque that rotates the angular momentum vector about the line of nodes, thereby changing  $i$ .

We re-cast equation (1) for our problem of a small body encountering a big body. For present purposes of illustration, we ignore  $\mathcal{O}(e)$  terms as small compared to unity, and ask how much the inclination changes after the small body has been accelerated for some time interval:

$$\Delta i = \sqrt{\frac{a}{Gm_*}} \int \frac{Gm_b}{|\mathbf{r}_b - \mathbf{r}|^2} f_N \cos u dt \quad (2)$$

where  $m_b$  is the big body mass,  $\mathbf{r} = x\hat{\mathbf{x}} + y\hat{\mathbf{y}} + z\hat{\mathbf{z}}$  and  $\mathbf{r}_b$  are the respective position vectors of the small and big bodies, and  $u \equiv \omega + f$  is the angle between the small body and the ascending node (also called the argument of latitude). The factor  $-1 \leq f_N \leq 1$  accounts for the component of the gravitational acceleration normal to the small body’s orbit:

$$f_N \equiv \frac{(\mathbf{r}_b - \mathbf{r}) \cdot \hat{\mathbf{l}}}{|\mathbf{r}_b - \mathbf{r}|} \quad (3)$$

where  $\hat{\mathbf{l}} = \sin i \sin \Omega \hat{\mathbf{x}} - \sin i \cos \Omega \hat{\mathbf{y}} + \cos i \hat{\mathbf{z}}$  is the unit orbit normal, and  $\Omega$  is the longitude of ascending node. Thus  $N = [Gm_b/|\mathbf{r}_b - \mathbf{r}|^2] f_N$  in eq. (2) is essentially the vertical acceleration. The factor of  $\cos u$  in eq. (2) accounts for the fact that  $N$  is most effective at changing  $i$  when it acts near the ascending or descending node ( $u \approx 0$  or  $\pi$ ); at these orbital phases,  $N$  can turn the velocity vector to change the magnitude of its vertical component,  $v_z$ . Put another way, near either node,  $v_z$  is at an extremum, and  $N$  can do work ( $\mathbf{N} \cdot \mathbf{v}_z \neq 0$ ) to change  $v_z$  (by contrast  $v_z = 0$  at  $u = \pm\pi/2$ ; here  $N$  changes  $\Omega$  but not  $i$ ). Thus the integral in eq. (2) yields the change  $\Delta v_z$ , which normalized by the Keplerian velocity  $v_K = \sqrt{Gm_*/a}$  gives  $\Delta i = \Delta v_z/v_K$ .

The sign of  $\Delta i$  can be positive or negative. Figure 3 illustrates both cases, for encounters near the crossing of the small body’s ascending node. In the left column, the small body is pulled downward harder post-node than it is pulled upward pre-node, and therefore  $\Delta i < 0$ . The right column shows the opposite case when  $\Delta i > 0$ .

### 2.2. How $\Delta i$ depends on $i$

The magnitude of  $\Delta i$  depends on  $i$ , as follows from eq. (3). For  $\mathbf{r}_b$  in the reference plane, the numerator of  $f_N$  scales as  $z$  and therefore  $i$  — a big body in the reference plane vertically accelerates a small body only when the latter is out of the reference plane. We may estimate the magnitude of  $f_N$  as:

$$|f_N| \sim \frac{|z|}{|\mathbf{r}_b - \mathbf{r}|} \sim \frac{ia}{\sqrt{e^2 + i^2}a} \quad (4)$$

for small  $i$  and  $e$  of the small body, and  $e_b = i_b = 0$  for the big body (the latter assumption may be relaxed as we do in later sections). For a picture, see Figure 4: the vertical component of the perturbation acceleration scales as the (sine of the) angle between the relative distance vector  $\mathbf{r} - \mathbf{r}_b$  and the reference plane; that angle is roughly equal to the small body’s vertical excursion (vertical epicyclic amplitude) divided by the total relative distance. The approximation  $|\mathbf{r}_b - \mathbf{r}| \sim \sqrt{e^2 + i^2}a$  is valid for the dispersion-dominated regime, when relative distances between bodies are dominated by epicyclic excursions (eccentricities, inclinations) and not by semimajor axis differences. Eq. (4) for  $|f_N|$  is a quick order-of-magnitude average over all possible encounter geometries;  $|f_N| \sim i/\sqrt{e^2 + i^2}$  uses maximum epicyclic excursion lengths ( $ia$  in the numerator and  $\sqrt{e^2 + i^2}a$  in the denominator) to establish scales, and does not literally assume that encounters occur only at moments of maximum epicyclic excursion.

Equation (4) indicates that if  $i \ll e$ ,  $f_N$  and by extension  $\Delta i$  scale as  $i$ . To verify this scaling, we



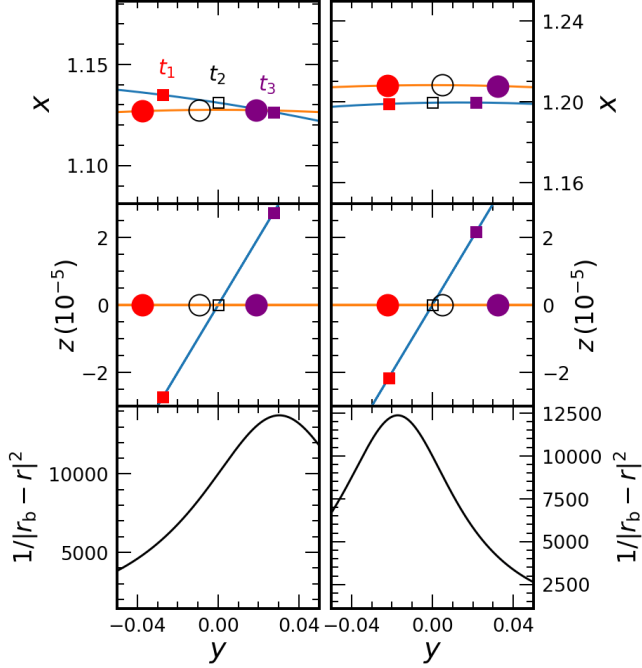


**Figure 3.** How close encounters between a small body (small square) and a big body (large circle) increase or decrease the small body’s orbital inclination. The big body is assumed for simplicity to reside on a circular orbit (orange line) in the reference plane, while the small body traces an eccentric orbit (blue line) which crosses the big body’s orbit (crossing is visible for the left column but not for the right), and whose ascending node is located on the  $x$ -axis at  $y = z = 0$ . The unit of length is arbitrary. Top and middle rows show zoomed-in face-on ( $x$ - $y$ ) and edge-on ( $z$ - $y$ ) views of the encounter at three times (colored red, open, and purple, consecutively) with the open symbols marking the moment when the small body crosses its node. The bottom panel shows the inverse square distance (measure of gravitational attraction) between the bodies as a function of the small body’s  $y$ -position. In the left column, the bodies are closest around  $t_3$  (purple) after the small body ascends above the big body — the net outcome is that the small body’s inclination will decrease, because it is overall pulled downward by the big body (the change in  $i$  is not shown). The opposite occurs in the right column, i.e. the small-body inclination increases, because the interaction is strongest before node crossing.

conduct the following experiment. We compute  $\Delta i$  using eq. (2) for a variety of encounter geometries, assuming for simplicity  $e_b = i_b = 0$ . As a control, we fix the in-plane impact parameter  $b_{\parallel} \equiv \sqrt{(x - x_b)^2 + (y - y_b)^2} = 0.001a$  at the moment the small body crosses the reference plane (either at the ascending or descending node), and fix also the small body eccentricity  $e = 0.1$ . The inclination  $i$  is varied systematically from  $10^{-5}$  to 0.1 rad, while all other angles (small-body periaapse longitude; small-body mean anomaly at node crossing; angular position of the big body relative to the small body at

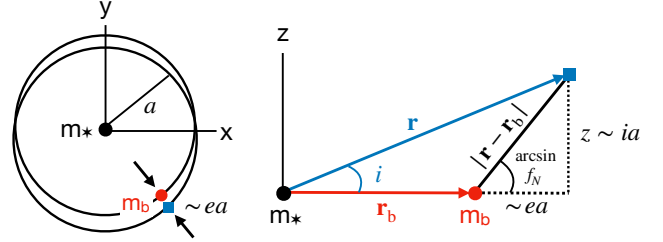


**Figure 4.** A big body of mass  $m_b$  (red circle) on a circular orbit in the  $x$ - $y$  reference plane encounters a small body (test particle, blue square) on a crossing orbit of eccentricity  $e$  and inclination  $i$ . The bodies have similar semimajor axes  $a$ . At the moment of encounter (conjunction), the small body feels a vertical gravitational acceleration which is less than the full gravitational acceleration by a factor of  $|f_N|$ , by definition. To order of magnitude,  $|f_N| \sim i/\sqrt{e^2 + i^2}$ .

node crossing) are drawn as uniform variates between 0 and  $2\pi$ . In calculating  $\Delta i$ , we restore the  $\mathcal{O}(e)$  and higher terms that we dropped in writing eq. (2), take the bodies to move on fixed Keplerian orbits (we do not update orbital elements on the fly), and integrate over a time interval centered on the moment of node crossing and over which the big body moves in mean longitude by  $\Delta\lambda_b = \pi$ . We have verified that the results for  $\Delta i$  are insensitive to the integration interval  $\Delta\lambda_b$  so long as the latter is on the order of unity.

For every input  $i$ , we compute  $\Delta i$  for 200 random orbital geometries. To within Poisson fluctuations,  $\Delta i$  is evenly distributed between positive and negative values. Figure 5 shows how the mean  $|\Delta i|$  varies with the input  $i$ , confirming that  $|\Delta i| \propto i$  for  $i \lesssim e$ .

We may also derive an order-of-magnitude version of equation (2) for  $|\Delta i|$ . Defining  $\mu_b \equiv m_b/m_*$ , and taking  $\cos u \sim 1$ , the encounter time  $\Delta t \sim b_{\parallel}/v_{\text{rel}}$ , and the relative encounter velocity  $v_{\text{rel}} \sim \sqrt{e^2 + i^2} v_K$ , we have:

$$\begin{aligned} |\Delta i| &\sim \frac{1}{v_K} \frac{Gm_b}{b_{\parallel}^2} \frac{b_{\parallel}}{\sqrt{e^2 + i^2} v_K} \frac{i}{\sqrt{e^2 + i^2}} \\ &= A_i \mu_b \frac{a}{b_{\parallel}} \frac{i}{e^2 + i^2} \end{aligned} \quad (5)$$

valid for  $\sqrt{e^2 + i^2} \gtrsim b_{\parallel}/a$  (since we have ignored the contribution to  $v_{\text{rel}}$  from the Keplerian shear), and  $i \lesssim e$  and both small. Equation (5) is simply the kick in vertical velocity  $\Delta v_z$  estimated using the impulse approximation ( $\Delta v_z \sim$  total gravitational acceleration  $\times$  encounter time  $\times f_N$  to account for the vertical component; see Fig. 4), normalized by the Kepler velocity to obtain  $|\Delta i|$ . We calibrate the fudge factor  $A_i \simeq 7$  using Fig. 5 (blue curve), and have verified numerically (with experiments similar to the ones underlying Fig. 5; data not shown) the scaling dependences of  $|\Delta i|$  on  $\mu_b$ ,  $b_{\parallel}$ , and  $e$  as given by

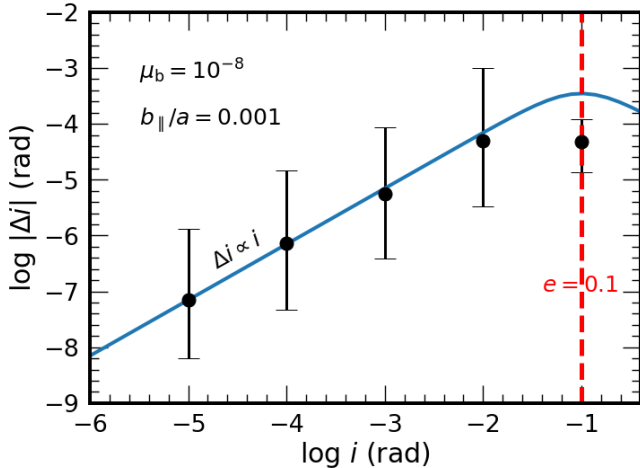


**Figure 5.** Magnitude of inclination change  $|\Delta i|$  of a small body encountering a big body, as a function of the pre-encounter mutual inclination  $i$ . The big body of mass  $\mu_b = m_b/m_* = 10^{-8}$  is assumed to have zero eccentricity. The test particle has eccentricity  $e = 0.1$ , and encounters the big body with an in-plane impact parameter ( $x$ - $y$  distance between the two bodies at  $z = 0$ ) fixed at  $b_{\parallel} = 0.001a$ . For each of 200 randomly chosen encounter geometries subject to the above conditions,  $|\Delta i|$  is computed by integrating Gauss’s perturbation equation (1) over a time interval centered on when the small body crosses  $z = 0$  (either ascending or descending), and of such duration that the big body moves in mean longitude by  $\Delta\lambda_b = \pi$ . Black points are mean values, and error bars extend from the 10th to 90th percentiles of the  $|\Delta i|$  distribution ( $\Delta i$  is evenly divided between positive and negative values modulo Poisson fluctuations). The blue curve is the order-of-magnitude estimate eq. (5),  $|\Delta i| = A_i \mu_b (a/b_{\parallel}) i / (e^2 + i^2)$ , with  $A_i = 7$  determined by eye. For  $i \ll e$ ,  $|\Delta i| \propto i$  — this is the “anisotropic” regime where the vertical component of the big body’s force scales as  $|f_N| = |z|/|\mathbf{r} - \mathbf{r}_b| \sim i/\sqrt{i^2 + e^2} \sim i/e$ . This linear relationship breaks down in the “isotropic” regime  $i \simeq e/2$ .

equation (5) — including the prediction that  $|\Delta i| \propto 1/i$  if  $e \sim i \gtrsim b_{\parallel}/a$ . We will return to this last result when we discuss in Section 2.5 how orbits evolve in equipartition.

The same reasoning that led to eq. (5) for  $|\Delta i|$  can be used to solve for  $|\Delta e|$ . Now only in-plane forces change the eccentricity, so we drop the factor of  $f_N$ :

$$\begin{aligned} |\Delta e| &\sim \frac{1}{v_K} \frac{Gm_b}{b_{\parallel}^2} \frac{b_{\parallel}}{\sqrt{e^2 + i^2} v_K} \\ &= A_e \mu_b \frac{a}{b_{\parallel}} \frac{1}{\sqrt{e^2 + i^2}} \end{aligned} \quad (6)$$

again valid for  $\sqrt{e^2 + i^2} \gtrsim b_{\parallel}/a$  (dispersion-dominated). Numerical experiments analogous to those underlying Fig. 5 verify the scaling dependences of eq. (6) and determine the fudge factor  $A_e \simeq 2.5$ .

### 2.3. Random walking in log inclination

We showed in the preceding subsection that in the anisotropic  $i \ll e$  regime,  $\Delta i \propto \pm i$ . Repeated scatterings cause the inclination to random walk, not with fixed steps of  $\Delta i$ , but with fixed steps of  $\Delta i/i = \Delta \ln i$ .

We conduct a random walk experiment with such logarithmic steps, analogous to the one we performed in Section 1 with linear steps that led to a Rayleigh inclination distribution. The random walk is in the 2D space  $(p, q) = (i \cos \Omega, i \sin \Omega)$ , because random perturbations in vertical velocity change both inclination  $i$  and nodal longitude  $\Omega$ . We start with 10000 particles with the same initial inclination  $i_0 = 10^{-2}$  rad and randomized nodes  $\Omega_0 \in [0, 2\pi)$ . For each random-walk step,  $(\Delta p, \Delta q) = (\Delta i \cos(\Omega - \Delta\Omega), \Delta i \sin(\Omega - \Delta\Omega))$ , with  $\Delta i/i = \Delta \ln i = 0.05$  and  $\Delta\Omega$  drawn as a uniform variate between 0 and  $\pi$  (not  $2\pi$ ). Our  $\Delta\Omega$  prescription is such that the nodal longitude  $\Omega$  decreases with every step, mimicking how an inclined particle nodally regresses when torqued by a perturber in the reference plane.<sup>1</sup> This prescription for the nodal evolution is just for illustration; other choices that preserve our assumed initial axisymmetry will give the same qualitative outcome, as we have tested. What is important is that the length of each step  $\Delta i = \sqrt{(\Delta p)^2 + (\Delta q)^2}$  scales with the length  $i = \sqrt{p^2 + q^2}$ , i.e. the inclination changes by a fixed fractional (not absolute) amount per step.

Figure 6 shows the inclination distribution of our 10000 particles after each has taken 1000 steps. Random walking in log space results in a log normal distribution, i.e. a Gaussian in log space. This is just the central limit theorem at work in log space. As with a random walk in linear space, here in log space the width of the Gaussian (measured in dex) grows as the square root of the number of steps. For this simple experiment, the log normal distribution remains centered on the initial inclination  $i_0$ ; this initial condition is not forgotten.

Unlike a Rayleigh distribution (Section 1), our log normal distribution does not reduce to  $i$  as  $i \rightarrow 0$ . A more realistic computation would account for a non-zero inclination dispersion for the big bodies. If  $i_b \neq 0$ , the actual inclination distribution of the small bodies when  $i < i_b$  (when the small bodies are immersed in the sea of big bodies) would differ from that computed here. In any case, it is the large  $i > i_b$  portion of the inclination

<sup>1</sup> From Gauss’s equation for  $d\Omega/dt \propto N \sin u$ , the particle’s node changes most for conjunctions with the perturber that occur when the particle attains maximum height above or below the perturber reference plane ( $u = \pm\pi/2$ ). At  $u = \pi/2$  the particle is pulled down by an in-plane perturber ( $N < 0$ ), and at  $u = -\pi/2$  the particle is pulled up ( $N > 0$ ). Either way,  $d\Omega/dt < 0$ .

distribution that matters for the wings of the vertical density profile. Our expectation of a log-normal shape to  $dN/di$  at large  $i$  will be confirmed in the  $N$ -body experiments of Section 3.

#### 2.4. Vertical density profile for a log normal inclination distribution

A simple way to obtain the vertical density profile  $dN/dz$  from the inclination distribution  $dN/di$  is to assume that every particle has the same semimajor axis ( $a = 1$  in arbitrary units) and zero eccentricity. Then for each of our 10000 particles we compute  $z = a \sin i \sin u$ , where  $u$  (the angular displacement of a particle from its ascending node) is drawn randomly from a uniform distribution between 0 and  $2\pi$ . The assumptions of fixed semimajor axis and zero eccentricity are made for simplicity; the numerical simulations in Section 3 will relax them, with no change in our conclusions.

Figure 7 shows the vertical density profile  $dN/dz$  derived from the log normal  $dN/di$  of Fig. 6, and fits  $dN/dz$  to both a Lorentzian and a Gaussian. The Lorentzian with its broader wings fits better. The broader wings in  $z$  follow from the log normal inclination distribution, whose large- $i$  tail is thicker than that of a linear Gaussian inclination distribution.

While we have so far only treated the case of big bodies on circular orbits, the same results should hold when  $e_b \neq 0$ , as long as the mutual inclination  $i \ll \max(e_b, e)$ . We will confirm this expectation with numerical integrations in Section 3. The anisotropic regime is generally defined as when the relative vertical (out-of-plane) motions are less than the relative horizontal (in-plane) motions. The former is controlled by the mutual inclination  $i$ , and the latter by a “mutual” eccentricity, which we can approximate as the quadrature sum of the small and big body eccentricities, or the maximum of the two, for random orbit orientations.

#### 2.5. Timescales for self-stirring, and big body masses

We estimate the time it takes small bodies to be stirred in  $i$  and  $e$  by a disk of big bodies of surface mass density  $\Sigma_b$ , assuming  $e_b \lesssim e$ .

A note on the validity of the results in this subsection: under the assumption  $e_b \lesssim e$ , the formulas derived here for  $e(t)$  of the small bodies can apply as well to the big bodies, as the big bodies (assuming there are more than one) eventually stir themselves at a rate equal to

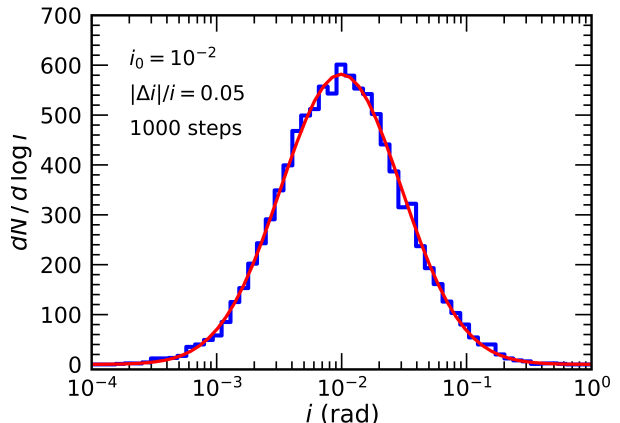


**Figure 6.** The inclination distribution of 10000 particles, initialized with  $i_0 = 10^{-2}$  and randomized nodes  $\Omega_0 \in [0, 2\pi)$ , after each has taken 1000 randomly directed steps in  $(p, q) = (i \cos \Omega, i \sin \Omega)$  space. Each step moves a particle by  $(\Delta p, \Delta q) = (\Delta i \cos(\Omega - \Delta \Omega), \Delta i \sin(\Omega - \Delta \Omega))$ , with  $\Delta i/i = \Delta \ln i = 0.05 = 0.021$  dex and  $\Delta \Omega$  chosen randomly from a uniform distribution between 0 and  $\pi$  (net regression; see main text). Data are shown as a blue histogram (logarithmically binned and not normalized), and the best-fit Gaussian in  $\log i$  is shown in red. The log normal distribution is centered on  $i_0$  (initial conditions are not forgotten) and we have verified that its width in  $\log i$  scales as the square root of the number of steps ( $\sqrt{1000} \times 0.021$  dex  $\simeq 0.67$  dex). Fixed  $\Delta \log i$  kicks arise when small bodies and big bodies cross orbits and  $i \ll e$  (Section 2), or when small bodies are radially separated from big bodies and  $i \ll |a - a_b|/a$  (see Appendix A).

that at which they stir small bodies.<sup>2</sup> In other words, the treatment in this subsection is for a “self-stirred” population of small and big bodies in which  $e(t) \approx e_b(t)$ . If instead  $e_b > e$  — say because the big body or bodies independently acquired a large  $e_b$ , e.g. by being scattered externally by another planet, and thrown into an initially more circular disk of small bodies (as may have happened for Neptune and the Kuiper belt; Nesvorný 2018; Huang et al. 2022) — then the formulas derived below for  $e(t)$  and  $i(t)$  would change, to keep track of which terms depend on  $e_b$  and which depend on  $e$ . We perform this calculation for  $e(t)$  and  $i(t)$  when  $e_b > e$  in Appendix C. Regardless, the main result of this paper, as contained in the preceding subsections of Section 2 and all of Section 3, that vertical Lorentzians arise when bodies are stirred

<sup>2</sup> This is not true at early times if  $e_b$  starts  $\ll e$ , when big bodies double their own eccentricities (over timescales that scale as  $e_b^4$ ) faster than they double the eccentricities of small bodies (over timescales that scale as  $e^4$ ; Section 2.5). But then  $e_b$  catches up to  $e$  and they grow thereafter at the same rate.

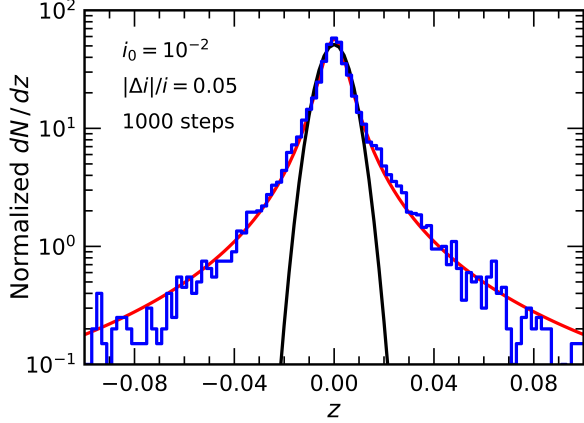


**Figure 7.** The log-normal  $dN/d\log i$  distribution of Fig. 6 yields a vertical density profile  $dN/dz$  (blue histogram, normalized) with broad wings. In computing  $dN/dz$ , we assume for simplicity that all particles have the same semimajor axis ( $a = 1$  in arbitrary units) and zero eccentricity; every particle in this narrow ring has a vertical position  $z = a \sin i \sin u$ , with  $u \in [0, 2\pi)$ . The best-fit Lorentzian (red) does better than the best-fit Gaussian (black) in fitting the vertical density profile. Side note: our bin sizes in  $z$  are small enough to resolve the central peak; the required bin size scales with the seed inclination  $i_0$ .

horizontally more than vertically ( $e_b, e \gg i$ ), holds independent of the origin and behavior of  $e_b$ .

A small body crosses vertically through the disk of big bodies (i.e. the reference plane) twice per orbit. Per plane crossing, the probability of a small body coming within impact parameter  $b_{\parallel}$  of a big body is given by the vertical optical depth of the big body disk,  $\tau = \pi b_{\parallel}^2 (\Sigma_b/m_b) \ll 1$  (where each big body is taken to have an encounter cross section  $\pi b_{\parallel}^2$ ). Then the time it takes a small body to come within  $b_{\parallel}$  of a big body is:

$$t_{b_{\parallel}} \sim \frac{2\pi}{n} \frac{1}{2\tau} \sim \frac{m_b}{n b_{\parallel}^2 \Sigma_b} \quad (7)$$

where  $n$  is the mean motion (orbital frequency) of the small body.

Each  $b_{\parallel}$ -encounter changes the small body inclination by  $\pm|\Delta i|$ , as given by eq. (5) when  $i \ll e$ . To double  $i$  — now interpreted as the small body rms dispersion — takes  $\sim (i/|\Delta i|)^2$  encounters:

$$t_{\text{double } i} \equiv \frac{i}{di/dt} \sim \left(\frac{i}{\Delta i}\right)^2 t_{b_{\parallel}} \sim \frac{e^4}{A_e^2} \frac{m_{\star}}{\Sigma_b a^2} \frac{1}{\mu_b} \frac{1}{n} \quad (8)$$

which is independent of  $b_{\parallel}$  — all encounters at various  $b_{\parallel}$  contribute equally to doubling  $i$ , implying eq. (8) should include a Coulomb-type logarithm ( $> 1$ ) in the

denominator.<sup>3</sup> Consistently, the same eq. (8) can be derived by asking how long it takes a small body to come sufficiently close to a big body that its inclination doubles. Set  $\Delta i \sim i$  in eq. (5) to solve for the required  $b_{\parallel}^* \sim c\mu_b a/e^2$ , and insert  $b_{\parallel}^*$  into eq. (7) to recover eq. (8).

The doubling time for  $i$  depends on  $e$ , which itself grows with time. By analogous reasoning now using eq. (6):

$$t_{\text{double } e} \equiv \frac{e}{de/dt} \sim \left(\frac{e}{\Delta e}\right)^2 t_{b_{\parallel}} \sim \frac{e^4}{A_e^2} \frac{m_{\star}}{\Sigma_b a^2} \frac{1}{\mu_b} \frac{1}{n} \quad (9)$$

which matches the variable scalings in the literature (e.g. eq. 4.2 of [Ida & Makino 1993](#) for how big bodies viscously stir the eccentricities of small bodies; or eq. 29 of [Goldreich et al. 2004](#)). Equation (9) may be solved for how eccentricity grows with time:

$$e(t) = e_0 (1 + t/T_0)^{1/4} \quad (10)$$

where

$$T_0 \equiv \frac{e_0^4}{4A_e^2} \frac{m_{\star}}{\Sigma_b a^2} \frac{1}{\mu_b} \frac{1}{n} \quad (11)$$

for an assumed initial condition  $e(t=0) = e_0$ . Inserting eq. (10) into eq. (8) allows us to solve for:

$$i(t) = i_0 (1 + t/T_0)^{A_i^2/(4A_e^2)} \quad (12)$$

for  $i(t=0) = i_0 \ll e_0$ . The exponent  $A_i^2/(4A_e^2)$  is nominally close to 2 but is uncertain because we have neglected order-unity factors in our derivation of eqs. (8) and (9) (e.g. Coulomb logs, which technically could differ between in-plane and out-of-plane stirring). As long as this exponent in  $i(t)$  exceeds the exponent of 1/4 in  $e(t)$ , inclination rises faster than eccentricity (assuming inclination starts much smaller than eccentricity, out of equipartition). That  $i$  increases faster than  $e$  is the same conclusion reached by [Goldreich et al. \(2004, their section 4.4.2\)](#) under dispersion-dominated conditions.

Given enough time,  $i$  will catch up to the equipartition value of  $e/2$ , after which both  $i$  and  $e$  grow in tandem as  $t^{1/4}$ , as follows from eqs. (5) and (6) which show that in equipartition,  $|\Delta i| \propto |\Delta e| \propto 1/i \propto 1/e$ . When in equipartition, the inclination and eccentricity

<sup>3</sup> It is called a Coulomb log because the same kind of logarithm appears when calculating bremsstrahlung emission from electron-proton scatterings in a plasma (e.g. [Rybicki & Lightman 1986](#)).



distributions follow Rayleigh distributions (e.g. [Ida & Makino 1992](#)).<sup>4</sup>

The time  $t_{\text{eq}}$  to reach equipartition depends on the unknowns  $i_0$  and  $e_0$ . By setting  $i(t)/e(t) = 1/2$  and solving for  $t = t_{\text{eq}}$ , we see that

$$t_{\text{eq}} = \left[ \left( \frac{e_0}{2i_0} \right)^{4/7} - 1 \right] T_0 \quad (13)$$

assuming  $A_i^2/(4A_e^2) = 2$  and  $e_0 > 2i_0$ . The time to equipartition scales especially strongly with  $e_0$  via eq. (11).

Unfortunately,  $e_0$  and  $i_0$  are not observables. To relate our theory to observables, we take the eccentricity solution eq. (10), set the elapsed time  $t$  equal to the system age  $t_{\text{age}}$ , and solve for  $t_{\text{age}}$  (following the same form as equation 9), assuming  $t_{\text{age}} \gg T_0$ :

$$t_{\text{age}} \sim \frac{e^4}{30} \frac{m_\star}{\Sigma_b a^2} \frac{1}{\mu_b} \frac{1}{n} \quad (14)$$

where  $e$  is the present-day eccentricity and the prefactor of 30 in the denominator is our guess for the product of  $4A_e^2$ , the Coulomb log, and other order-unity factors we have neglected. What is attractive about working with the eccentricity eq. (10) and its corollary eq. (14) is that the dependence on the unknown initial condition  $e_0$  drops out. The same is not true working with the inclination solution eq. (12), which depends on  $e_0$  and  $i_0$  and is further marred by its uncertain exponent. More physically, eq. (14) follows from the eccentricity doubling time eq. (9), which shows that the doubling time increases steeply as  $e^4$ . Thus the last doubling of  $e$  takes longest, and to order of magnitude we may set  $t_{\text{age}}$  equal to the time it takes to double up to the present-day  $e$  (as given by the right-hand side of eq. 9), recovering eq. (14).

Given a big body mass  $m_b = \mu_b m_\star$ , equation (14) may be solved for the total (collective) mass in big bodies, in a disk annulus of area  $2\pi a \Delta a$ :

$$M_{\text{b,tot}} \simeq 2\pi \Sigma_b a \Delta a \sim \frac{2\pi e^4}{30} \frac{\Delta a}{a} \frac{1}{n t_{\text{age}}} \frac{m_\star}{m_b} m_\star$$

<sup>4</sup> Our equipartition scaling  $|\Delta i| \propto 1/i$  differs from the assumption of fixed  $|\Delta i|$  made in Section 1 to derive a Rayleigh distribution. But the difference is not important for deriving a Rayleigh distribution. The central limit theorem yields Gaussians (or on a sphere, Rayleigh distributions) when the random-walk steps are drawn from any probability distribution with finite variance. The equipartition scaling  $|\Delta i| \propto 1/i$  satisfies the condition of finite variance — it leads to smaller random-walk steps at higher  $i$ , shrinking the width of the distribution function (unlike the anisotropic scaling  $|\Delta i| \propto i$ ). We have verified that if instead of fixing  $|\Delta i|$  we draw  $|\Delta i|$  from a probability distribution extending over the interval  $(c_1, c_1 + c_2/i)$  for positive constants  $c_1$  and  $c_2$  ( $c_1 \neq 0$  since the  $1/i$  scaling breaks down at small  $i$ ), we recover a Rayleigh distribution (data not shown).

$$\begin{aligned} & \sim 400 M_\oplus \left( \frac{e}{0.1} \right)^4 \left( \frac{\Delta a/a}{0.2} \right) \left( \frac{100 \text{ Myr}}{t_{\text{age}}} \right) \\ & \times \left( \frac{a}{100 \text{ au}} \right)^{3/2} \left( \frac{0.002 m_\oplus}{m_b} \right) \left( \frac{m_\star}{m_\odot} \right)^{3/2} \end{aligned} \quad (15)$$

where we have normalized the right-hand side using Pluto-like big bodies with  $m_b = 0.002 m_\oplus$ .

The largest possible big-body mass,  $\max m_b$ , is the same as the smallest possible total mass,  $\min M_{\text{b,tot}}$ , and corresponds to having a single big body in the disk annulus:

$$\begin{aligned} \max m_b &= \min M_{\text{b,tot}} \\ & \sim \left( \frac{2\pi e^4}{30} \frac{1}{n t_{\text{age}}} \frac{\Delta a}{a} \right)^{1/2} m_\star \\ & \sim 1 M_\oplus \left( \frac{e}{0.1} \right)^2 \left( \frac{\Delta a/a}{0.2} \right)^{1/2} \left( \frac{100 \text{ Myr}}{t_{\text{age}}} \right)^{1/2} \\ & \times \left( \frac{a}{100 \text{ au}} \right)^{3/4}. \end{aligned} \quad (16)$$

In Section 4, we will evaluate eqs. (15) and (16) for real-life debris disks.

### 3. NUMERICAL EXPERIMENTS

To test our analytic ideas, we conduct numerical experiments with the  $N$ -body code **REBOUND** ([Rein & Liu 2012](#)), outfitted with the hybrid-symplectic **MERCURIUS** integrator that can treat close encounters ([Rein et al. 2019](#); [Tamayo et al. 2020](#)). We simulate how one or two big bodies gravitationally stir a narrow annulus of small bodies (test particles), with the aim of finding out-of-equipartition situations where in-plane relative velocities greatly exceed out-of-plane velocities. Under such circumstances, according to the theory of Section 2, test particles should be stirred into vertical Lorentzians, or at least into profiles with broader wings than Gaussians. Such non-Gaussian profiles are also expected to morph into Gaussians, as particles eventually relax into equipartition.

The simulation parameters (orbital radii, perturber masses, run times), though reminiscent of those in real-life debris disks, are chosen more for computational convenience, as our goal for this section is not to model observations, but to test theory.

#### 3.1. Numerical set-up

The big bodies, numbering one or two in a given simulation, each have mass  $m_b = \mu_b m_\odot = 1.5 \times 10^{-8} m_\odot$

**Table 1.** Stirring simulations

(1)	(2)	(3)	(4)	(5)	(6)	(7)	(8)	(9)	(10)
Run	$\mu_b$	$a_b$	$a_{\text{init}}$	$e_b$	$e_{\text{init}}$	$i_b$	$i_{\text{init}}$	L or G ( $e_{\text{med}}/i_{\text{med}}$ )	L or G ( $e_{\text{med}}/i_{\text{med}}$ )
	( $10^{-8}$ )	(au)	(au)			(rad)	(rad)	@ $t = 1$ Myr	@ $t = 20$ Myr
A	1.5	30	30.154	0.1	0	0	$10^{-5}$	L (0.009/0.001)	L (0.037/0.004)
A-low	1.5	30	30.154	0.1	0	0	$10^{-6}$	L (0.010/0.0001)	L (0.040/0.004)
B	1.5	30	30.154	0.1	0.1	0	$10^{-5}$	L (0.100/0.001)	L (0.101/0.005)
C	1.5	30	30.154	0	0.1	0	$10^{-5}$	L (0.100/0.001)	L (0.101/0.005)
D	1.5	30	30.154	0	0.02	0	$10^{-5}$	L (0.024/0.002)	G (0.021/0.010)
E	1.5	30	30.154	0	0	0	$10^{-5}$	—	L (0.011/0.0002)
AA	1.5, 1.5	30, 30	30.154	0.1, 0.1	0	$0, 10^{-4}$	$10^{-5}$	L (0.004/0.001)	L (0.015/0.004)
AA-low	1.5, 1.5	30, 30	30.154	0.1, 0.1	0	$0, 10^{-5}$	$10^{-5}$	L (0.009/0.001)	L (0.020/0.004)
BB	1.5, 1.5	30, 30	30.154	0.1, 0.1	0.1	$0, 10^{-4}$	$10^{-5}$	L (0.100/0.001)	L (0.101/0.004)
CC	1.5, 1.5	29.959, 30.349	30.154	0, 0	0.1	0, 0	$10^{-5}$	L (0.100/0.001)	L (0.101/0.006)
DD	1.5, 1.5	29.959, 30.349	30.154	0, 0	0.02	0, 0	$10^{-5}$	L (0.024/0.003)	G (0.022/0.009)
EE	1.5, 1.5	29.959, 30.349	30.154	0, 0	0	0, 0	$10^{-5}$	L (0.011/0.003)	G (0.016/0.008)

NOTE—Columns: (1) Run name. (2) Ratio of big body mass to central mass (for reference, the mass of Pluto relative to the Sun is  $6.6 \times 10^{-9}$ ). In the case of two big bodies, there are two entries. (3) Initial big body semimajor axis or axes. (4) Initial semimajor axis of test particles, typically 3 big-body Hill radii away from the big body. Initial mean anomalies of test particles are drawn from a uniform variate  $[0, 2\pi)$ . (5) Initial big body eccentricity. In the case of 2 big bodies, both initial particle longitudes and initial periape longitudes are  $180^\circ$  apart. (6) Initial eccentricity of test particles. Initial periape longitudes of test particles are drawn from a uniform variate  $[0, 2\pi)$ . (7) Initial big body inclination. (8) Initial inclination of test particles. Initial nodal longitudes of test particles are drawn from a uniform variate  $[0, 2\pi)$ . (9) Whether the vertical distribution of test particles  $dN/dz$  resembles more a Lorentzian (L) or a Gaussian (G), at simulation time  $t = 1$  Myr. For Run E, test particle inclinations at  $t = 1$  Myr remain mostly unchanged from their initial values and therefore the vertical density profile at this time is not usefully obtained. Also listed in parentheses are the median eccentricity  $e_{\text{med}}$  and median inclination  $i_{\text{med}}$  of test particles at  $t = 1$  Myr, computed for  $i > 10 i_{\text{init}}$  to minimize contamination from initial conditions. (10) Same as (9) but for  $t = 20$  Myr.

(about  $2 \times$  Pluto’s mass), and orbit the central  $m_\star = m_\odot$  star with semimajor axis  $a_b \simeq 30$  au (similar to Neptune’s orbit). The big bodies stir  $N = 10000$  nearby test particles, initialized with small non-zero inclinations relative to big bodies to seed the vertical stirring. Simulations are run for 20 Myr, comparable to the ages of the ARKS III debris disks studied in this paper (Section 4).

Table 1 compiles input parameters. Run names take a single letter for simulations with only one big body, and two letters for two big bodies. Between runs, the main parameters we focus on varying are the initial eccentricities, either of the big bodies ( $e_b$ ) or the small bodies ( $e_{\text{init}}$ ). For a given run,  $e_b$  and  $e_{\text{init}}$ , and the inclinations  $i_b$  and  $i_{\text{init}}$  (relative to a reference plane coinciding with a big body orbit plane), are set to constants listed in Table 1 — in a given run, the test particle orbits are all initialized with the same  $e_{\text{init}}$  and  $i_{\text{init}}$ , and differ only in their nodal and periape longitudes, and mean anomalies. Large initial

eccentricities and small inclinations set the stage for anisotropic, out-of-equipartition dynamics.

In line with the rest of this paper, we simulate dispersion-dominated, i.e. orbit-crossing conditions. We focus on the orbital evolution of small bodies as they scatter off big bodies, whose own orbits are constructed to not change much, keeping the experiments as controlled as possible. In runs with only one big body (whose orbit cannot change), the test particle semimajor axes are all initialized with the same  $a_{\text{init}} = a_b + 3R_H$ , where  $R_H = (\mu_b/3)^{1/3} a_b$  is the big body Hill radius. These test particle semimajor axes lie just within the big body’s chaotic zone (whose half-width is about  $2\sqrt{3}R_H \simeq 3.5R_H$ ; Gladman 1993; Chambers et al. 1996; Pearce et al. 2024; cf. Wisdom 1980), which leads to strong scatterings and orbit crossings even when orbits are not initially crossing. In some runs the bodies start on eccentric and crossing orbits. When two (identical) big bodies are present with circular orbits, they are initialized with semimajor axes that are 6 mutual Hill radii apart ( $6 \times 2^{1/3}R_H$ ), with

all test particles initialized with the same semimajor axis exactly midway. While the test particles scatter chaotically onto crossing orbits, the big bodies are far enough apart that they do not perturb one another much. For runs with two big bodies on eccentric crossing orbits, the initial eccentricities  $e_b = 0.1$  are large enough that eccentricity doubling times exceed the duration of the simulation (see eq. 9).

### 3.2. Results of numerical simulations

We mostly review the runs with two big bodies, as their results are simpler to analyze. The results for runs with just one big body reinforce the results with two big bodies, but have some extra (mostly distracting) features, in retrospect stemming from our simplifying assumption of a single big body. We shunt these single big body technicalities to Appendix B.

Table 1 summarizes run outcomes. For runs with two big bodies, we find that  $e_b = 0.1$  or  $e_{\text{init}} = 0.1$  (Runs AA, AA-low, BB, CC) yield  $dN/dz$  profiles after 20 Myr that are better fitted to Lorentzians than Gaussians. By comparison, when  $e_b$  and  $e_{\text{init}}$  are  $\leq 0.02$  (Runs DD, EE), the vertical profiles are more Gaussian at 20 Myr. When examining the vertical profiles, we omit particles with  $i < 10 i_{\text{init}}$ , as these have inclinations too close to their assumed initial value and are considered “unstirred”. Our goal with these numerical experiments is to discover what vertical profiles result from viscous stirring (again, not to model observations), and to that end we need to sample only stirred (scattered) particles. For the simulations showcased in this section (Runs BB and DD), and most of the simulations in Table 1, the unstirred particles constitute less than a few percent of all particles at  $t = 1$  Myr, and much less than a percent at  $t = 20$  Myr (precise percentages are given in figure captions).

Notably, in all runs, including those where the outcomes are ultimately Gaussian, the vertical profiles sampled at an earlier time  $t = 1$  Myr are Lorentzian. For all our initial conditions, test particle random motions start out of equipartition ( $e \gg 2i \rightarrow$  Lorentzian  $dN/dz$ ). Particles then evolve toward equipartition ( $e = 2i \rightarrow$  Gaussian  $dN/dz$ ), with runs starting closer to equipartition achieving it by their ends.

Table 1 lists median eccentricities  $e_{\text{med}}$  and median inclinations  $i_{\text{med}}$  of test particles at  $t = 1$  and 20 Myr. We elect to tabulate the medians and not the rms (root-mean-squared) values, as the former are less sensitive to outlier events (ejections). Nevertheless we have also tabulated rms values (data not shown); they are larger than the medians, especially for inclination, but tell the same story as the median values: when  $e \simeq 2i$ , we find

vertical Gaussian profiles, and where  $e \gg 2i$ , we find vertical Lorentzians.

Figures 8–10 describe Run BB where equipartition is never reached. The vertical density profiles at  $t = 1$  and 20 Myr are approximately Lorentzian, with the profile at the later time just starting to relax toward a Gaussian (Fig. 8). The inclination distribution at 20 Myr is intermediate between that of a log normal and a Rayleigh distribution (Fig. 9), with the log normal better describing those large  $i$  particles that dominate the thick tails of the vertical density profile. Eccentricities at 20 Myr remain considerably larger than inclinations (Fig. 10).

Figures 11 and 12 describe Run DD where a Lorentzian holds at  $t = 1$  Myr, but not at  $t = 20$  Myr when test particles have relaxed into equipartition ( $e \simeq 2i$ ) and the vertical density profile is Gaussian.

Similar results are obtained for the single big body experiments: compare the all-Lorentzian runs initialized with  $e_b, e_{\text{init}} = 0.1$  for which  $e_b, e > 2i$  (Runs A, A-low, B, C), against the early-Lorentzian, late-Gaussian Run D initialized with  $e_b = 0$  and  $e_{\text{init}} = 0.02$  for which  $e > 2i$  at  $t = 1$  Myr, and  $e \simeq 2i$  at  $t = 20$  Myr. Run A-low is initialized with a smaller  $i_{\text{init}}$  than Run A, but the results at  $t = 20$  Myr are practically indistinguishable. Additional technical details about Runs A, B, C, and D are relegated to Appendix B.

Runs E and EE initialize both small and big bodies with zero eccentricity, and consequently  $e$ 's and  $i$ 's take longer than in other runs to grow. At  $t = 1$  Myr in Run E, test particle inclinations remain largely at their initial values and a measurement of the vertical density profile at this time is not meaningful. At  $t = 1$  Myr in Run EE, and  $t = 20$  Myr in Run E, the  $e$ 's and  $i$ 's have grown, with  $e \gg 2i$  and the vertical density profiles exhibiting Lorentzians (Table 1). From these results we infer that when eccentricities are initially zero and inclinations are non-zero but small, the eccentricities at first grow faster than and leapfrog over the inclinations; this is consistent with how viscous stirring under shear-dominated (sub-Hill) conditions excites eccentricities more than inclinations (Goldreich et al. 2004). Eventually though, as the particles become dispersion-dominated (super-Hill), the inclinations catch up, as demonstrated by Run EE at  $t = 20$  Myr (see also Section 2.5).

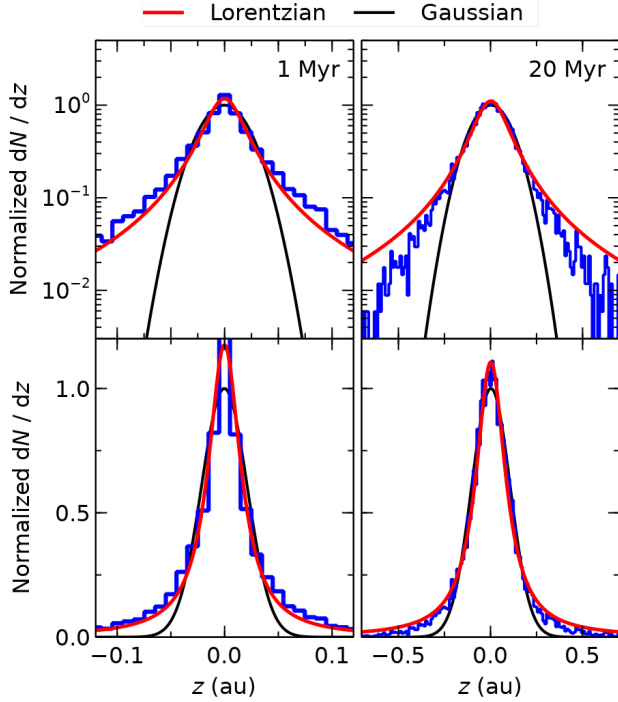


**Figure 8.** Vertical density profiles of test particles (a.k.a. small bodies) simulated with REBOUND in Run BB, sampled at  $t = 1$  Myr (left column) and 20 Myr (right). Log and linear scalings are shown on top and bottom rows, respectively; a linear scaling is more fairly compared to the ALMA observations for which measured disk surface brightness contrasts do not exceed a factor of  $\sim 10$  (see their Fig. 1). Run BB features small bodies (test particles) and two big bodies all with initial eccentricities = 0.1, much larger than their mutual inclinations of  $10^{-5}$ – $10^{-4}$  rad; accordingly, in-plane relative velocities between big and small bodies well exceed out-of-plane relative velocities most of the time. Under such circumstances big bodies force small bodies to take inclination steps  $\Delta i \propto \pm i$  (Section 2), and small-body vertical distributions (blue histograms) should resemble Lorentzians (red curves) more than Gaussians (black curves). By  $t = 20$  Myr the test particles have begun to transition from a Lorentzian to a Gaussian. Test particles having  $i < 10 i_{\text{init}} = 10^{-4}$  (constituting 4.9% of all test particles at  $t = 1$  Myr, and 0.06% at 20 Myr) have been omitted as these reflect too strongly our assumed initial inclinations. The horizontal axis changes scale by a factor of 5 between left and right columns as the disk thickens vertically with time.

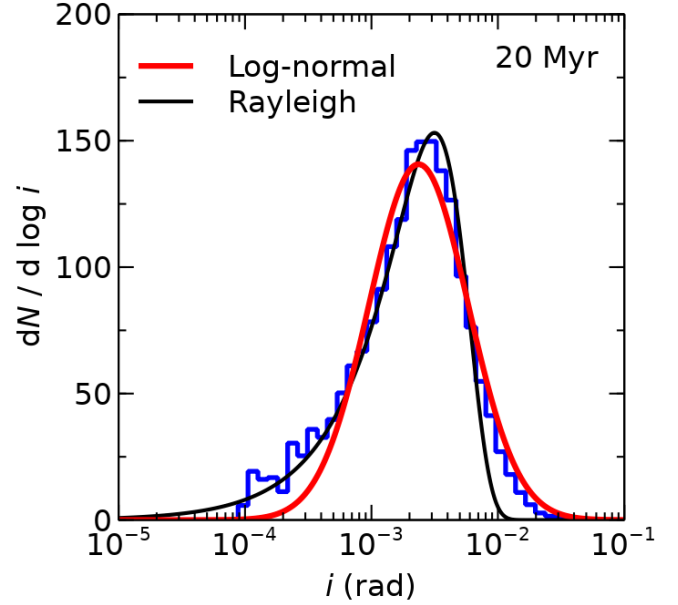


**Figure 9.** Inclination distribution of test particles for Run BB (two big bodies with  $e_b = \{0.1, 0.1\}$ , and test particles on initially eccentric  $e_{\text{init}} = 0.1$  orbits with small seed mutual inclinations of  $10^{-5}$ – $10^{-4}$  rad relative to big bodies) at  $t = 20$  Myr (blue histogram). Overlaid are a best-fit log normal distribution (red curve) and a Rayleigh distribution (black curve). The log normal fits better for large  $i$ , while Rayleigh fits better for small.



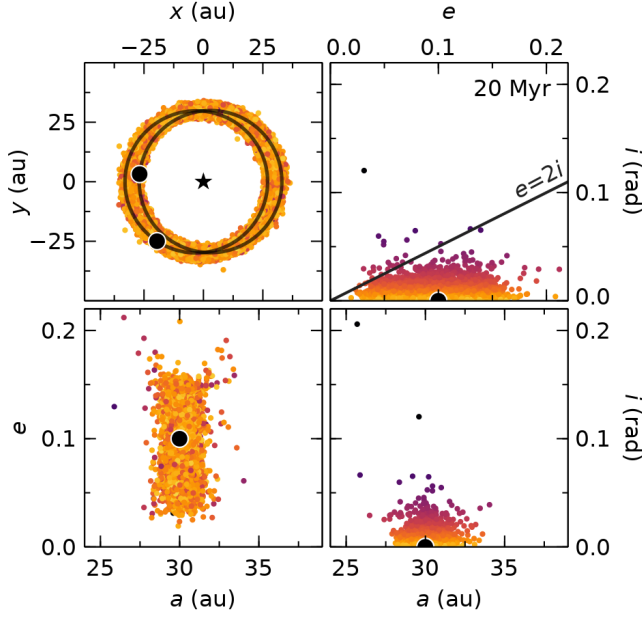


**Figure 10.** Orbital elements for Run BB (two big bodies with  $e_b = 0.1, 0.1$ , test particles on initially eccentric  $e_{\text{init}} = 0.1$  orbits with small seed mutual inclinations of  $10^{-5}$ – $10^{-4}$  rad) at  $t = 20$  Myr. In all panels, test particles are represented by colored points, and big bodies are represented by black discs. *Top left:* Snapshot of test particles, big bodies and their orbits, and the host star in the  $x$ - $y$  plane. *Top right:* Inclinations  $i$  vs. eccentricities  $e$  for big bodies and test particles. The test particle points are colored according to their inclinations; the same color scheme is used for all panels. The  $e = 2i$  line marks equipartition between in-plane and out-of-plane motions; most bodies, including the big bodies, lie below this line (i.e.  $i < e/2$ ), as required for small-body kicks  $|\Delta i|$  to scale as  $i$  (Section 2). *Bottom left:* Eccentricities  $e$  vs. semimajor axes  $a$ . *Bottom right:* Inclinations  $i$  vs. semimajor axes  $a$ .

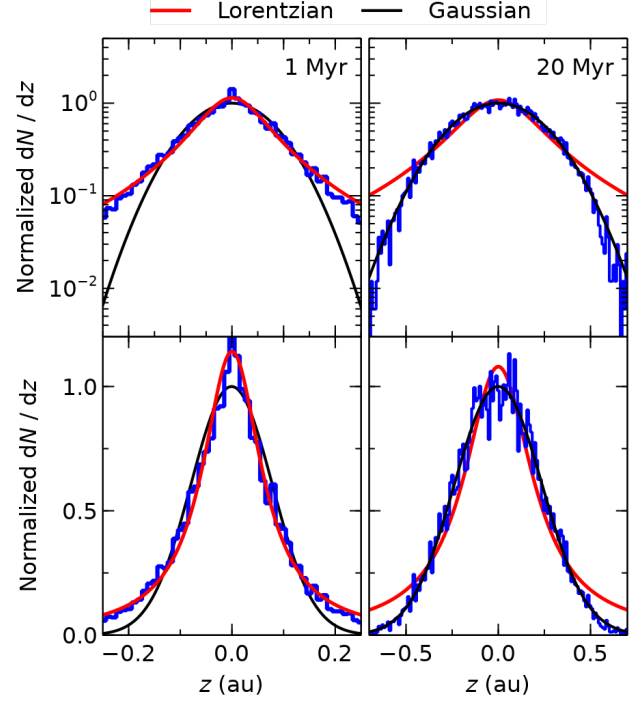


**Figure 11.** Vertical density profiles of test particles simulated with REBOUND in Run DD which contains two big bodies on circular orbits ( $e_b = \{0, 0\}$ ) and initially low-eccentricity test particles ( $e_{\text{init}} = 0.02$ ). Compared to Run BB (Figs. 8–10) which has larger starting eccentricities, here for Run DD mutual inclinations become comparable to eccentricities at earlier times. At  $t = 1$  Myr (left panel), the vertical profile of test particles (blue histogram) matches a Lorentzian (red curve). By  $t = 20$  Myr (right panel), the vertical distribution has equilibrated to a Gaussian (black curve). Test particles having  $i < 10 i_{\text{init}} = 10^{-4}$  (constituting 2.2% of all test particles at  $t = 1$  Myr, and 0.01% at 20 Myr) have been omitted as these reflect too strongly our assumed initial inclinations.

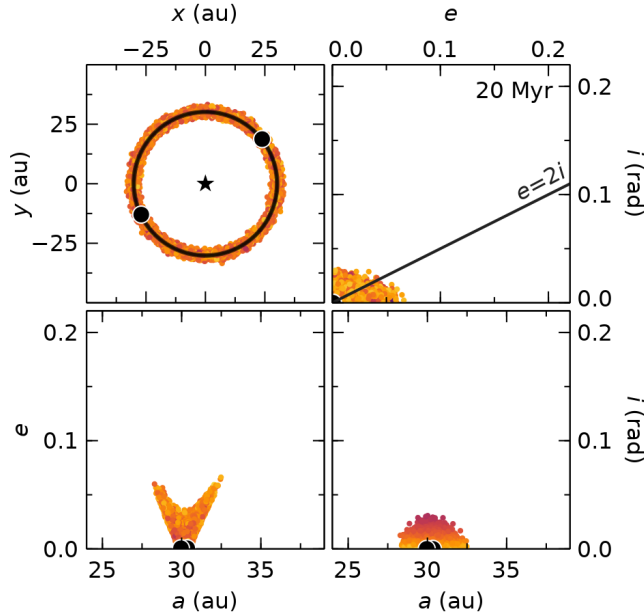


**Figure 12.** Orbital elements for Run DD (two big bodies on initially circular orbits  $e_b = 0, 0$ , test particles with initially low eccentricities  $e_{\text{init}} = 0.02$ ), sampled at  $t = 20$  Myr. In all panels, test particles are represented by colored points, and the big bodies are represented by black discs. *Top left:* Snapshot of test particles, big bodies and their orbits, and the host star in the  $x$ - $y$  plane. *Top right:* Inclinations  $i$  vs. eccentricities  $e$  of big bodies and test particles. The test particle points are colored according to their inclinations; the same color scheme is used for all panels. Most of the test particles are distributed about the  $e = 2i$  line indicating equipartition between in-plane and out-of-plane random motions. *Bottom left:* Eccentricities  $e$  vs. semimajor axes  $a$ . *Bottom right:* Inclinations  $i$  vs. semimajor axes  $a$ .

To close out this section, we show in Figure 13 how the median eccentricities and inclinations of our test particles evolve with time, for the same runs featured in previous figures. As noted above, while both medians and rms values yield qualitatively similar outcomes, we found the medians to be less sensitive to ejections and to better represent the majority of particles making up the bulk of the vertical profile. As anticipated from Section 2, inclinations (either median or rms) grow faster than eccentricities. In Run DD, which exhibits a vertical Gaussian at late times,  $i$  catches up to  $e$  to within a factor of 2, eventually growing as  $t^{1/4}$  as expected in equipartition. As the energies in motions parallel and perpendicular to the midplane are exchanged, inclinations grow at the expense of eccentricities — the decrease in  $e$  is most visible at late times when  $i$  is largest. In Run BB which features vertical Lorentzians at all times, inclinations also grow but remain smaller than eccentricities by more than a factor of 2.

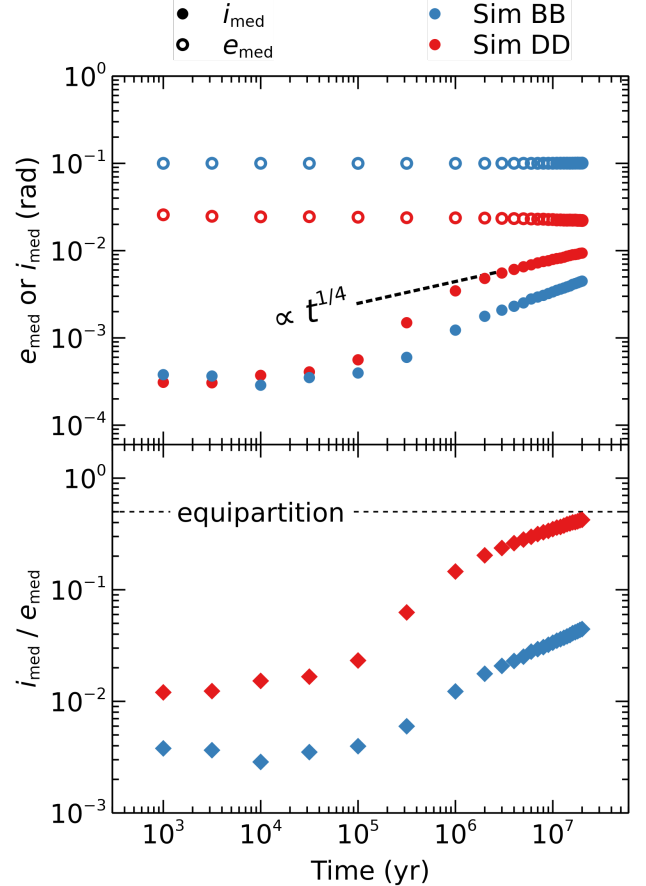


**Figure 13.** Median  $e$  and median  $i$  of test particles vs. time for the same runs shown in previous figures. Inclinations rise faster than eccentricities. In Run DD,  $i$  catches up to within a factor of 2 of  $e$  and eventually grows as  $t^{1/4}$  as  $i/e$  nears the equipartition value of  $1/2$  (dotted line); accordingly, the particles in DD conform to a vertical Gaussian at late times (Fig. 11). The median  $e$  decreases as the median  $i$  increases, reflecting how relative motions parallel to the disk midplane are re-directed into perpendicular motions as equipartition is approached. Inclinations in Run BB also grow but fall short of eccentricities by more than a factor of 2; the corresponding vertical profiles are Lorentzian-like (Fig. 8).

#### 4. APPLICATION TO REAL-LIFE DISKS

We apply the stirring theory of Section 2 and in particular the self-stirring theory of Section 2.5 to estimate the individual and collective masses of big bodies within ARKS III debris disks, as observed in the mm continuum. We restrict consideration to radially narrow disks having annular widths  $\Delta R$  less than  $0.5 \times$  their mean orbital radius  $R$ , since their dynamics should be local and simpler to interpret (see also Section

**Table 2.** Radially narrow debris disks from ARKS III

(1)	(2)	(3)	(4)	(5)	(6)	(7)	(8)	(9)	(10)	(11)
Disk ID	Vertical form	$M_\star$ ( $M_\star$ )	$t_{\text{age}}$ (Myr)	$R$ (au)	$\Delta R_{\text{FWHM}}$ (au)	$\Delta R_{\text{FWHM}}/R$	$h_{\text{HWHM}}$	$i$	$e$	$\max m_b = \min M_{\text{b,tot}}$ ( $M_\oplus$ )
HD 15115	vL	1.426	45	80.7	14	0.17	0.021	0.025	0.1	1.3
HD 32297	vL	1.57	30	115.9	37	0.32	0.0098	0.012	0.047–0.16	0.69–7.9
HD 61005	vL	0.95	45	72.4	36	0.50	0.0129	0.015	0.062–0.25	0.59–9.5
HD 197481 (AU Mic)	vL	0.614	23	33.6	13	0.39	0.0026	0.003	0.012–0.193	0.012–2.9
HD 109573	vG	2.14	10	75.9	7	0.09	0.0065	0.0078	0.016	0.065
HD 131488	vG	1.804	16	89.7	13	0.14	0.0048	0.0058	0.012	0.035

NOTE—Columns: (1) Disk name. (2) Best-fitting vertical profile from ARKS III, vL = Lorentzian, vG = Gaussian. (3) Host stellar mass (ARKS I). (4) System age (ARKS I). (5) Disk radius, as determined from fits to mm-wave continuum images assuming the dust surface density follows a single Gaussian in orbital radius (ARKS I). For HD 15115, two Gaussians (separated in radius by  $\sim 30\%$ ; see e.g. ARKS III Table A.1) are required to fit the visibilities, and the tabulated  $R$  is the average of their centers (ARKS I). (6) Disk annular width, as measured by the full width at half-maximum (FWHM) of an assumed Gaussian dust surface density in radius (ARKS I). For HD 15115, two Gaussians are needed to fit the data, and the reported  $\Delta R$  is the sum of their widths. (7) Disk fractional width in radius. (8) Best-fit disk aspect ratio  $h_{\text{HWHM}} \equiv H_{\text{HWHM}}/R$  from ARKS III (their Table 2), where  $H_{\text{HWHM}}$  is the vertical height where the dust density falls to half its midplane value. (9) Inclinations of disk particles estimated as  $i = h_{\text{HWHM}}/\sqrt{\ln 2}$  (formally valid for rms  $i$  and vertical Gaussians) (10) Eccentricities of disk particles (free components only), either equal to the equipartition value of  $2i$  if the disk is vertically Gaussian (vG), or ranging from  $e_{\text{min}} = 4i$  (eq. 18) to  $e_{\text{max}} = 0.5 \Delta R_{\text{FWHM}}/R$  (eq. 19) for vertically Lorentzian (vL) disks. For HD 15115,  $e_{\text{min}} = 0.1$  and  $e_{\text{max}} = 0.09$  and so we set  $e = 0.1$ . (11) Big body mass  $m_b$  in the case where there is only one big body stirring the entire disk. This is also the same as the minimum total mass in big bodies  $M_{\text{b,tot}}$ , since  $M_{\text{b,tot}} \propto 1/m_b$  according to the viscous stirring relation eq. (14). Ranges in  $\max m_b = \min M_{\text{b,tot}}$  are shown for those Lorentzian disks with a range of eccentricities between  $e_{\text{min}}$  (eq. 18) and  $e_{\text{max}}$  (eq. 19).

5.2). Table 2 lists those disks with measured aspect ratios  $h_{\text{HWHM}}$  from ARKS III, and  $R$  and  $\Delta R_{\text{FWHM}}$  from ARKS I. The latter derive from parametric fits to dust surface densities assumed to be radially Gaussian. While more complicated radial structures were considered by ARKS II (Han et al. 2026b) and ARKS III, all fitting methods agree that the sources listed in Table 2 can be described as radially narrow rings. The two neighboring rings detected in HD 15115 have been merged into one for simplicity (ARKS I); our conclusions about this system do not change qualitatively were we to keep the rings separate.

Our inferences about big bodies rest on equation (14) which provides a joint constraint on the surface density of big bodies  $\Sigma_b$  and the mass of an individual big body  $m_b$ , assuming the ring is self-stirred with big body eccentricities  $e_b \lesssim e$  (see beginning of Section 2.5). From  $\Sigma_b$  we may estimate the collective ring mass in big bodies as  $M_{\text{b,tot}} = 2\pi\Sigma_b R\Delta R_{\text{FWHM}}$  (eq. 15). The constraint in eq. (14) depends strongly on the present-day eccentricity  $e$ , interpreted as the quadrature sum of the small and big body eccentricities (see discussion between eqs. 15 and 16). Equation (14) states that these eccentricities

(and by extension mutual inclinations) are the direct result of in-situ viscous stirring by big bodies over a time equal to the system age  $t_{\text{age}}$ . It further assumes that collisional damping of eccentricities and inclinations is negligible. The no-damping assumption is valid when collisional strengths  $Q^*$  are small compared to the square of relative velocities  $v_{\text{rel}}^2$  in the collisional cascade, so that bodies of a given mass fragment from collisions with projectiles of much smaller mass. Such high-mass-ratio collisions do not damp relative velocities efficiently (Jankovic et al. 2024; Jankovic et al. 2026). Whether the no-damping condition holds is model-dependent, and damping might actually be significant for the smallest eccentricities (smallest  $v_{\text{rel}}$ ) we consider. Nevertheless insofar as collisional damping is expected to drive disks to equipartition and thereby relax into vertically Gaussian profiles, the Lorentzian disks in our sample evidently escaped damping.

As described so far, our procedure is largely identical to the one carried out by Jankovic et al. (2026; see also Matrà et al. 2019 and Pearce et al. 2025). Their equation (20) (taken from Ida & Makino 1993) matches our equation (14) to within an order-unity factor. The

main difference between our procedures is in how  $e$  is evaluated.

We estimate  $e$  differently depending on whether a disk is observed to exhibit a Lorentzian or Gaussian vertical profile. For the two Gaussian (“vG”) disks in Table 2 (HD 109573 and HD 131488), we assume, like Jankovic et al. (2026), equipartition:

$$e = 2i = 2\sqrt{2}h_\sigma = \frac{2}{\sqrt{\ln 2}} h_{\text{HWHM}} \quad (\text{vertical Gaussian}) \quad (17)$$

where  $e$  and  $i$  are here formally their rms values, and we have distinguished between the disk scale height measured as a standard deviation ( $h_\sigma$ ), and as a half width at half maximum ( $h_{\text{HWHM}}$ ) (Matrà et al. 2019; Ida & Makino 1992). For the four Lorentzian (“vL”) disks (HD 15115, HD 32297, HD 61005, and HD 197481 a.k.a. AU Mic), we are led by the theory of Section 2 to believe that  $e > 2i$ , i.e. inclinations and eccentricities are out of (not yet in) equipartition. Accordingly, we still take  $i = \sqrt{2}h_\sigma$ ,<sup>5</sup> but now consider a range of eccentricities between

$$\begin{aligned} e_{\min} &\equiv 2 \times 2i = 4\sqrt{2}h_\sigma \\ &= \frac{4}{\sqrt{\ln 2}} h_{\text{HWHM}} \quad (\text{vertical Lorentzian}) \end{aligned} \quad (18)$$

and

$$e_{\max} = 0.5 \times \Delta R_{\text{FWHM}}/R \quad (\text{vertical Lorentzian}) \quad (19)$$

(see Table 2). For HD 15115,  $e_{\min} = 0.10$  and  $e_{\max} = 0.09$ , and so for this disk we set  $e = 0.1$ . Allowing for a range of eccentricities from  $e_{\min}$  to  $e_{\max}$  is where we differ from Jankovic et al. (2026), who instead use the equipartition relation (eq. 17) for all disks regardless of whether they better fit vertical Lorentzians or Gaussians. (Their sample size is also larger, as they do not select for radially narrow disks.) Our use of  $e_{\max}$  to derive a maximum  $M_{\text{b,tot}}$  as a function of  $m_{\text{b}}$  is the same procedure used by Pearce et al. (2025) to constrain the big body properties in the Fomalhaut debris disk; our resultant formulas (their eq. 5 vs. our eq. 15 with eq. 19 inserted) differ only by an order-unity factor.

A final note on  $e$  as it has been used throughout this paper: these are free eccentricities, not forced eccentricities. The latter refer to mean values characterizing globally eccentric disks such as

<sup>5</sup> Technically the  $\sqrt{2}$  applies only to Gaussian profiles, but we adopt it anyway for convenience and so that our Lorentzian and Gaussian treatments share a common reference.

Fomalhaut (e.g. Kalas et al. 2005; MacGregor et al. 2017; Lovell et al. 2025). For the disks in our sample, Lovell et al. (2026, ARKS VI; and references therein) measured forced eccentricities of  $\sim 0.1$  for HD 109573,  $> 0.03$  for HD 32297, and  $> 0.02$  for HD 15115. These forced eccentricities are not directly relevant here because they refer to mean orbital streamlines that do not cross. We are concerned instead with gravitational scatterings in the dispersion-dominated, orbit-crossing regime, where relative velocities are controlled by free (a.k.a. proper) eccentricities (e.g. Murray & Dermott 1999).

#### 4.1. Constraints on individual and collective big body masses in ARKS III disks

Using equations (14)–(19) and the data in Table 2, we compute for each disk the possible combinations of collective ring mass  $M_{\text{b,tot}}$  vs. individual big body mass  $m_{\text{b}}$ , and display these in Figure 14. For each disk with a definite  $e$  (HD 15115, plus the two vG disks assumed to be in equipartition), the possible combinations of  $M_{\text{b,tot}}$  vs.  $m_{\text{b}}$  trace a line of slope -1 ( $M_{\text{b,tot}} \propto 1/m_{\text{b}}$ ). For each Lorentzian disk having a range of possible non-equipartition  $e$ ’s, the possibilities for  $M_{\text{b,tot}}$  vs.  $m_{\text{b}}$  fill a 2D region that is bounded from above by the slope -1 line for  $e = e_{\max}$ , and from below by the slope -1 line for  $e = e_{\min}$ . Our Figure 14 should be compared with the colored lines in Figure 8 of Jankovic et al. (2026); quantitatively there are differences for individual sources, but overall the orders of magnitude spanned by  $m_{\text{b}}$  and  $M_{\text{b,tot}}$  overlap between our respective studies.

At large  $m_{\text{b}}$ , every slope -1 line in Fig. 14 is capped on the right at the  $M_{\text{b,tot}} = m_{\text{b}}$  dashed line, corresponding to the case where a given disk contains just a single big body. This single big body mass ranges from  $\sim 10^{-2} m_{\oplus}$  (about a lunar mass; the bottom-most point for AU Mic) to  $\sim 10 m_{\oplus}$  (about a super-Earth or sub-Neptune; the right-most points for HD 32297 and HD 61005).

Each slope -1 line in Fig. 14 is capped on the left at small  $m_{\text{b}}$  such that the collision time between big bodies equals the system age. Including gravitational focussing, the collision time is estimated as

$$t_{\text{col}} = \frac{1}{\eta_{\text{b}} \times \pi (2s_{\text{b}})^2 [1 + 4Gm_{\text{b}}/(s_{\text{b}}v_{\text{rel}}^2)] \times v_{\text{rel}}} \quad (20)$$

where the volumetric number density of big bodies is

$$\eta_{\text{b}} = \frac{M_{\text{b,tot}}}{m_{\text{b}}} \frac{1}{2\pi R \Delta R_{\text{FWHM}} \times iR}, \quad (21)$$

the big body radius is  $s_{\text{b}} = [3m_{\text{b}}/(4\pi\rho_{\text{b}})]^{1/3}$  for internal density  $\rho_{\text{b}} = 3 \text{ g/cm}^3$ , and the relative velocity between



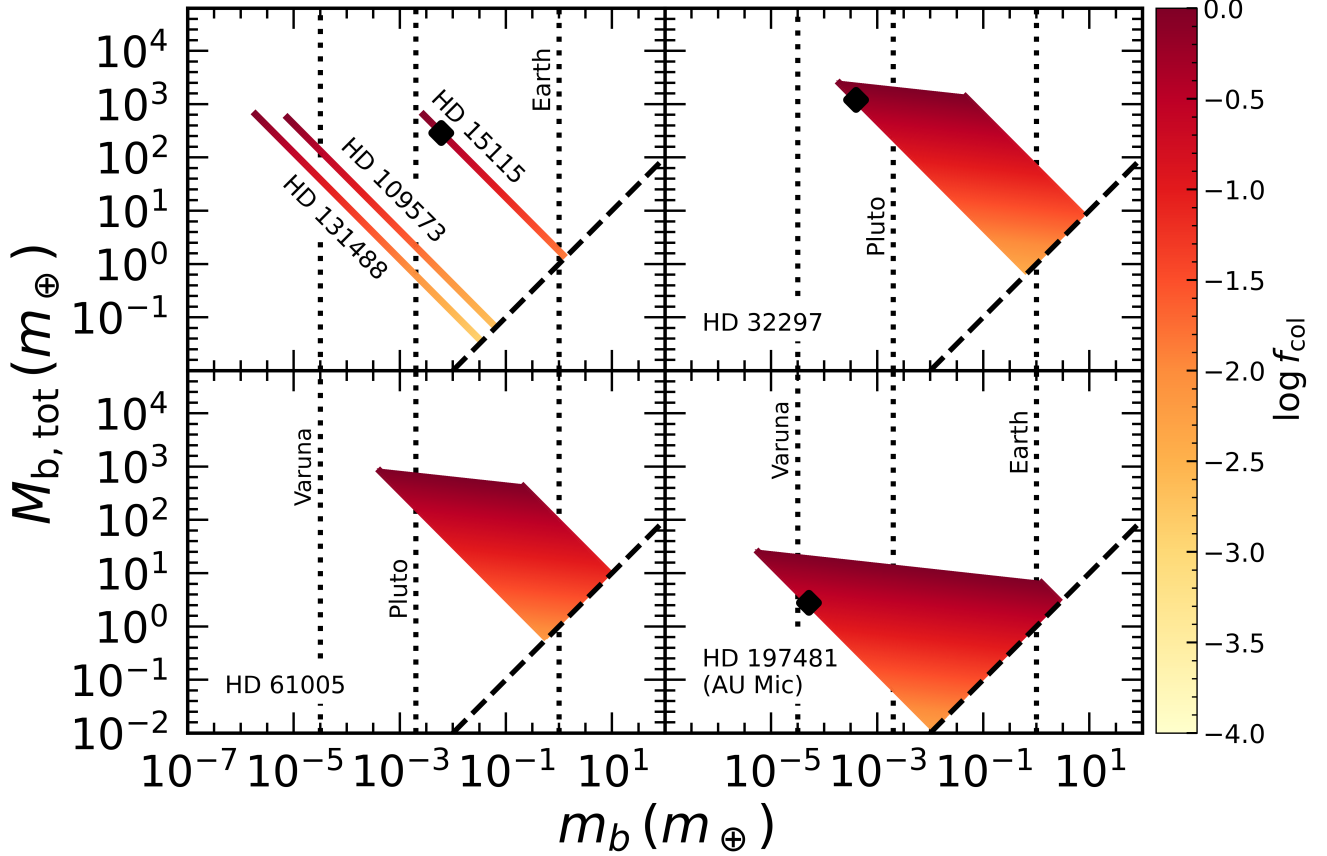


**Figure 14.** Possible individual big body masses  $m_b$ , and total masses in all big bodies  $M_{b,\text{tot}} = 2\pi\Sigma_b R\Delta R_{\text{FWHM}}$ , for the six radially narrow rings in Table 2. All loci are computed from eq. (14) which states that a given disk’s present-day free eccentricities  $e$  result from viscous self-stirring over the disk age  $t_{\text{age}}$ , with no collisional damping (free eccentricities are distinct from any forced value characterizing globally eccentric disks like Fomalhaut). The free eccentricity is estimated from its equipartition value ( $2i$ , where  $i = h_{\text{HWHM}}/\sqrt{\ln 2}$  and  $h_{\text{HWHM}}$  is an observationally fitted disk aspect ratio) for vertically Gaussian disks HD 109573 and HD 131488. For the vertically Lorentzian disks HD 15115, HD 32297, HD 61005, and HD 197481 (AU Mic),  $e$  is bounded by the out-of-equipartition values  $e_{\text{min}}$  (eq. 18) and  $e_{\text{max}}$  (eq. 19). In the case of HD 15115 for which  $e_{\text{min}} = 0.1$  and  $e_{\text{max}} = 0.09$ , we set  $e = 0.1$ . For each of the three disks with definite  $e$  (top left panel), the loci of possibilities is a line of slope -1, since  $M_{b,\text{tot}} \propto m_b^{-1}$  by eq. (15). Each line starts at top left at the value of  $m_b$  for which the fraction  $f_{\text{col}}$  of big bodies colliding over  $t_{\text{age}}$  equals one (see color bar), and ends at bottom right at the  $m_b = M_{b,\text{tot}}$  dashed line corresponding to a single big body. Each of the other disks (top right and bottom panels) features a continuum of slope -1 lines, each line corresponding to a different  $e > 2i$ . The disks HD 15115, HD 32297, and AU Mic are claimed to exhibit the remains of recent catastrophic disruptions of dwarf planets (Jones et al. 2023; Chiang & Fung 2017). For these disks we indicate with black diamonds the combinations of  $m_b$ ,  $M_{b,\text{tot}}$  that generate enough debris in erosive collisions to supply the mass being ground down in standard collisional cascades, as constrained by disk brightnesses at infrared to mm-wave wavelengths (Jankovic et al. 2026). See Table 3 for the full set of parameters, and Figure 15 for a companion plot.

big bodies is

$$v_{\text{rel}} = \sqrt{(5/4)e^2 + i^2} \sqrt{\frac{Gm_{\star}}{R}} \quad (22)$$

(Lissauer & Stewart 1993).<sup>6</sup> Gravitational focussing is important for our parameter space ( $4Gm_{\text{b}}/s_{\text{b}} > v_{\text{rel}}^2$ ); dropping the +1 in the brackets in eq. (20), we find that along each slope -1 line, the collision time  $t_{\text{col}} \propto m_{\text{b}}^{2/3}$ . A lower bound on  $m_{\text{b}}$  is obtained by requiring  $t_{\text{col}} > t_{\text{age}}$ , since otherwise the big body stirrers would completely obliterate themselves (mostly in mergers; see Section 4.2). Thus the loci of possibilities plotted in Fig. 14 are capped at low  $m_{\text{b}}$  (high  $M_{\text{b,tot}}$ ) such that the collision probability

$$f_{\text{col}} = \frac{t_{\text{age}}}{t_{\text{col}}} \quad (23)$$

equals 1. How  $f_{\text{col}} \propto 1/m_{\text{b}}^{2/3}$  decreases from 1 as  $m_{\text{b}}$  increases is encoded in color in Fig. 14. We have found that the lower bound on  $m_{\text{b}}$  derived from  $f_{\text{col}} = 1$  is larger (more constraining) than the one usually adopted in the literature, that the surface escape velocity from the big body equals  $v_{\text{rel}}$  (e.g. Daley et al. 2019).

#### 4.2. Sourcing the collisional cascade by eroding big body stirrers

The self-stirring constraints in Fig. 14 allow for collective big body masses  $M_{\text{b,tot}}$  approaching  $\sim 10^3 m_{\oplus}$ , up to the limit of what is plausible on cosmogonic/planet formation grounds (Krivov & Wyatt 2021). These same large values of  $M_{\text{b,tot}}$  also have the largest collisional probabilities  $f_{\text{col}}$ . Thus it seems possible that in this region of parameter space, big bodies colliding over the system age may contribute significantly to the collisional cascades that must be present in debris disks. Bodies at the top of such “standard” cascades have estimated sizes of  $\sim 10$  m to 10 km, and continuously grind down to produce the small bodies observable from  $\mu\text{m}$  to mm wavelengths (e.g. Pan & Sari 2005; Wyatt et al. 2011; Krivov & Wyatt 2021; Jankovic et al. 2026). The total cascade mass  $M_{\text{cascade}}$  (i.e. the amount of mass ground down over the system age = the mass at the top of the cascade) can range from  $\sim 0.01 m_{\oplus}$  (AU Mic) to  $\sim 10^2 m_{\oplus}$  (Jankovic et al. 2026, the data points in their Figure 8).

We consider here the possibility that collisionally eroding some of the big body stirrers can feed the

observable small body cascade. By “eroding” we mean that only a small fraction of the mass in a given pair of colliding big bodies will be released as debris. In the allowed parameter space in Fig. 14, big body collisions are gravitationally focussed: the velocity at impact equals the mutual surface escape velocity. Assuming the big bodies are big enough to be held together by their own internal gravity (as opposed to their “strength” in intermolecular bonds), such strongly focussed collisions result predominantly in mergers, i.e. accretion. Only a small fraction  $f_{\text{debris}}$  of the colliding mass escapes as ejecta; as the impact angle ranges from  $0^\circ$  (head-on collisions) to  $90^\circ$  (grazing),  $f_{\text{debris}}$  varies from  $\sim 10\%$  to 0 (e.g. Emsenhuber et al. 2020, their Figure 5, right panel).

The rate at which the big body stirrers collisionally inject debris into the disk is  $f_{\text{debris}} \times M_{\text{b,tot}}/t_{\text{col}}$  — this formula holds even when  $t_{\text{col}} > t_{\text{age}}$ , which is the regime in which we are using it — and can in principle match the rate at which mass is ground into observable small bodies in the standard cascade. Indeed three of the disks in our sample — HD 197481 (AU Mic), HD 32297, and HD 15115 — have been argued based on their scattered-light morphologies to contain the recently shattered remains of dwarf planets (Chiang & Fung 2017; Jones et al. 2023). In this vein we present Figure 15, which is the same as Figure 14 except that it color-codes the allowed parameter space by the total number of big body collisions occurring within the system age:

$$N_{\text{col}} = f_{\text{col}} \frac{M_{\text{b,tot}}}{m_{\text{b}}} . \quad (24)$$

For each of the three aforementioned candidate giant impact disks, we mark with a diamond in Fig. 15 the specific parameter space where the mass in debris released over the system age

$$M_{\text{big body debris}} = f_{\text{debris}} N_{\text{col}} m_{\text{b}} \quad (25)$$

approaches the cascade mass  $M_{\text{cascade}}$  calculated by Jankovic et al. (2026, their Figure 8). We assume throughout  $f_{\text{debris}} = 3\%$ . For AU Mic,  $M_{\text{cascade}} \sim 0.025\text{--}0.05 m_{\oplus}$  in “boulders”  $\sim 3\text{--}20$  m in radius (Jankovic et al. 2026; see also Strubbe & Chiang 2006 for a similar cascade mass estimate). We find that if  $M_{\text{b,tot}} = 3 m_{\oplus}$  and  $m_{\text{b}} = 5 \times 10^{-5} m_{\oplus}$ , then  $N_{\text{col}} \sim 10^4$  and  $M_{\text{big body debris}} \sim 0.02 m_{\oplus}$ , comparable to  $M_{\text{cascade}}$ . The above value for  $m_{\text{b}}$  is comparable to that of the Kuiper belt object Varuna (volume-equivalent diameter of 700 km and internal density of 1 g/cc; Fernández-Valenzuela

<sup>6</sup> Equation (22) for  $v_{\text{rel}}$  is derived for big bodies in equipartition. For bodies that are out of equipartition, corrections to eq. (22) should only alter the coefficients for  $e^2$  and  $i^2$  by factors of order unity.

et al. 2019).<sup>7</sup> In other words, in this region of allowed parameter space, collisionally merging  $N_{\text{col}} \sim 10^4$  viscously stirring Varunas over  $t_{\text{age}} \sim 23$  Myr produces  $\sim 0.02 m_{\oplus}$  of boulders that can feed the collisional cascade in AU Mic. See Table 3 for a summary of these parameters.

For HD 15115 and HD 32297, analogous agreement between  $M_{\text{big body debris}}$  and  $M_{\text{cascade}}$  (now ranging from  $\sim 5$  to  $60 m_{\oplus}$ ) can be obtained for big bodies on the order of Pluto in size (Table 3). These calculations illustrate the potential for the big body stirrers to source a healthy fraction and perhaps even all of the observable cascade. For HD 32297, the collision frequency of big bodies (sub-Plutos) can be remarkably high, occurring on average once every  $\sim 20$  years. Again, as these are strongly gravitationally focussed collisions, they result in mergers with  $f_{\text{debris}}$  of just a few percent, not catastrophic disruptions (see footnote 7).

## 5. SUMMARY AND DISCUSSION

As particles in a disk gravitationally scatter off one another (these can be solid particles in a circumstellar debris disk or planetary ring, or stars in a galactic disk), their eccentricities  $e$  and inclinations  $i$  diffuse. Working in the dispersion-dominated regime where bodies are on crossing orbits, with relative velocities controlled by  $e$  and  $i$  and not by the background shear, we have shown that when  $e \gg i$ , i.e. when relative velocities between particles are much larger parallel to the disk midplane than perpendicular, particles are gravitationally (“viscously”) stirred into vertical density distributions resembling Lorentzians.

Vertical Lorentzians result from particles random walking in inclination  $i$  such that their individual steps  $\Delta i \propto \pm i$ . Such a scaling is obviously true when  $i = 0$ , and arises because changes in inclination depend on the vertical component of the gravitational acceleration

between scattering particles. That vertical component increases as the angle  $f_N$  (technically  $\arcsin f_N$ ) between the line joining two scattering particles and the midplane horizontal (Equation 3 and Figure 4); in turn,  $f_N$  increases with the mutual inclination  $i$  (Equation 4). Thus the steps  $\Delta i$  do not have constant magnitude but rather have constant  $\Delta i/i = \Delta \ln i$ . A random walk with fixed steps in  $\log i$  generates a log normal inclination distribution  $dN/di$ , whose thick tail at high  $i$  produces the broad Lorentzian-like wings of the disk’s vertical density profile  $dN/dz$ .

Given enough dispersion-dominated scatterings, inclinations grow to catch up to eccentricities, and the system relaxes into equipartition with  $e \simeq 2i$ . At this stage, the random-walk steps  $\Delta i$  stop exponentiating (the angle  $f_N$  saturates at order unity) and the vertical density profile  $dN/dz$  relaxes to a Gaussian.

We have reached these conclusions informally and empirically, by semi-analytic reasoning and  $N$ -body integrations. Conceivably our results could be obtained formally. One could, for example, compute analytically the sky-projection integral that transforms an inclination distribution  $dN/di$  to a vertical density profile  $dN/dz$  (e.g. section 5.1 of Matrà et al. 2019). Or one could try to relate our findings to the generalized central limit theorem which shows how Gaussians and Lorentzians arise from sampling distributions with finite and infinite variance, respectively (e.g. Feller 1971; Bouchaud & Georges 1990; see also the Holtsmark distribution reviewed by Chandrasekhar 1943). Vertical density profiles, in real life and in our numerical computations, only approximate Gaussians or Lorentzians over limited ranges in height, so care needs to be taken when connecting reality to analytics and formal theorems which may only be true asymptotically, in the limit of infinite sample sizes. These explorations are left for the future.

In related work, Collins & Sari (2006) and Collins et al. (2007) solved a Boltzmann-like equation to derive broad, non-Rayleigh distributions for eccentricity in planar, viscously stirred, shear-dominated particle disks. While our focus has been on the vertical dynamics of dispersion-dominated disks where relative velocities between bodies are not controlled by the background shear, we also found that log normal inclination distributions and by extension vertical Lorentzians can arise in shear-dominated disks, for non-crossing scattering bodies separated in semimajor axis by  $|a - a_b| \gg ia$  (Appendix A). In shear-dominated disks,  $e$  grows faster than  $i$  and therefore  $e \gg i$  naturally (e.g. Goldreich et al. 2004; Collins & Sari 2006). But typical debris disks are not shear-dominated; for observed disk parameters, there is no set of perturbing “big body” masses and surface densities consistent with

<sup>7</sup> The recent destruction of a Varuna-like body of mass  $\sim 10^{-4} m_{\oplus}$  was proposed by Chiang & Fung (2017) to explain AU Mic’s escaping dust clouds as seen in scattered light (Boccaletti et al. 2015, 2018). But the colliding Varunas that we are presently considering result in mergers and percent-level erosion of mass, not the kind of catastrophic disruption envisioned by Chiang & Fung (2017). It might be possible to modify their scenario to create a Varuna’s worth of dust from the collisional merger of bodies  $1/f_{\text{debris}} \sim 30\times$  more massive than Varuna. Such larger bodies would be more numerous and collide more frequently in a viscous stirring model that included collisional damping of small body eccentricities and inclinations (see Jankovic et al. 2026 for such a model; our models assume no damping).

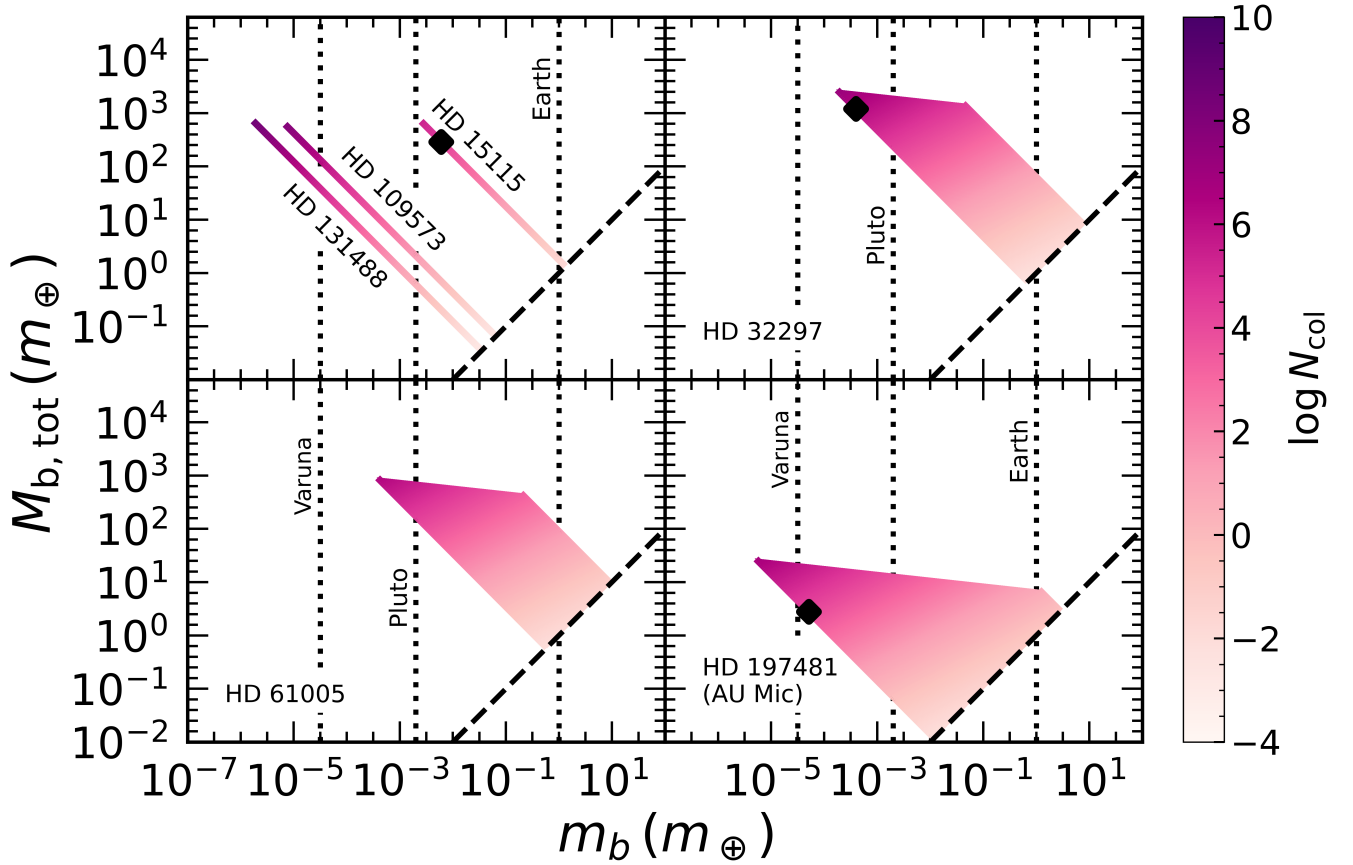


**Figure 15.** Same as Fig. 14, but now color-coded according to  $N_{\text{col}}$ , the number of big body collisions occurring over  $t_{\text{age}}$ . Black diamonds mark where there are sufficient collisions ( $N_{\text{col}}$  of order  $10^4$  for HD 15115 and AU Mic, and  $10^6$  for HD 32297; see Table 3 for more precise values) that the mass  $M_{\text{big body debris}}$  eroded from big bodies over the system age approaches the mass  $M_{\text{cascade}}$  ground down into small dust grains observed at  $\mu\text{m}$  to  $\text{mm}$  wavelengths (Jankovic et al. 2026). Similar estimates hold for the other disks in the figure, but we highlight HD 15115, HD 32297, and AU Mic because they are candidate disks for hosting the remains of recent giant impacts (Jones et al. 2023; Chiang & Fung 2017).

shear-dominated stirring explaining present-day vertical thicknesses (Jankovic et al. 2026).

### 5.1. Anisotropic viscous stirring in ARKS III debris disks: dynamical and collisional masses

Most of the debris disks studied in ARKS III (Zawadzki et al. 2026) have vertical Lorentzian profiles, which could imply they are out of equipartition, with  $e \gg 2i$ . How can such anisotropic conditions prevail under dispersion-dominated conditions? We have no definite answer and can only outline some general considerations. The hypothesis we have adopted throughout this paper is that Lorentzian disks arrive (somehow) dispersion-dominated and anisotropic, and are not old enough to have relaxed into equipartition. The relaxation time starting from some initial eccentricity  $e_0$  is roughly equal to the

time it takes to double that eccentricity, and increases steeply with it (eqs. 10–12 and surrounding discussion). Imaged debris disks are located in the outermost regions of planetary systems, and here large eccentricities are especially plausible because local orbital velocities are small and easier to change. If there were a single big body/planet viscously stirring the disk, one can imagine its eccentricity having been excited externally by another planet, either secularly or in a prior episode of planet-planet scattering — much like Neptune, or some “rogue” planet since lost from the outer solar system, is thought to have been temporarily scattered by neighboring giant planets into the Kuiper belt, stirring it into its present hot state (e.g. Nesvorný 2018; Huang et al. 2022; see also our Appendix C). A single eccentric big body would also force a global eccentricity on the surrounding disk



**Table 3.** Big body properties that can source collisional cascades in giant impact candidate disks

(1)	(2)	(3)	(4)	(5)	(6)	(7)	(8)
Disk ID	$m_b$	$M_{b,tot}$	$N_{col}$	$t_{age}/N_{col}$	$f_{col}$	$M_{big\ body\ debris}$	$M_{cascade}$
	( $m_{Pluto}$ )	( $m_{\oplus}$ )		(yr)		( $m_{\oplus}$ )	( $m_{\oplus}$ )
HD 15115	3	300	$3 \times 10^4$	$2 \times 10^3$	54%	5	5–15
HD 32297	0.2	1200	$2 \times 10^6$	20	57%	21	20–60
HD 197481 (AU Mic)	0.025	3	$1 \times 10^4$	$2 \times 10^3$	21%	0.02	0.025–0.05

NOTE—Columns: (1) Disk name. These disks are the subset of radially narrow ARKS III disks (Table 2) proposed to exhibit the remains of giant impacts as traced by non-axisymmetric shapes in scattered light (Jones et al. 2023; Chiang & Fung 2017). (2) Individual big body mass (in units of Pluto’s mass  $m_{Pluto} = 0.002 m_{\oplus}$ ), chosen specifically to yield  $M_{big\ body\ debris} \sim M_{cascade}$ . (3) Collective big body mass integrated over the entire disk. (4) Number of big body collisions occurring over the system age  $t_{age}$ . (5) Average time between big body collisions. (6) Fraction of big bodies that collide over the system age. (7) Estimated mass in debris from big body collisions over the system age ( $M_{big\ body\ debris} = M_{b,tot} f_{col} f_{debris}$ ), assuming each collision releases a mass fraction  $f_{debris} = 3\%$  in ejecta. (8) Mass in the “standard” collisional cascade producing small bodies observable from  $\mu\text{m}$  to mm wavelengths, calculated by Jankovic et al. (2026, their Figure 8). The range reflects different assumptions about the slope of the size distribution.

of observable small bodies, even as it crosses orbits with disk particles (e.g. Fig. 19 in Appendix B). Lovell et al. (2026, ARKS VI) present a number of disks with global eccentricities.

Alternatively, big bodies could grow their own eccentricities by viscously stirring themselves, in situ. Under the “self-stirring” hypothesis of Section 2.5, where big bodies stir each other and the smaller observable dust grains at identical rates, we estimated the numbers and masses of big bodies needed to stir each of six radially narrow debris disks from ARKS III to their current inclinations and eccentricities. The more massive the individual perturbers, the fewer of them are required (the total number of big bodies scales as the inverse square of the individual big body mass). On one end of the allowed parameter space, there could be a small ensemble of large perturbers ranging in individual mass from a lunar mass (e.g. in AU Mic) to a super-Earth/sub-Neptune (e.g. in HD 32297 and HD 61005; Section 4 and Table 2). The number of such large perturbers could be so few (potentially as low as one) that they would not collide with one another over the system age.

On the other end of the allowed parameter space, disks could be self-stirred by a large number (up to tens of millions if not more) of smaller stirrers, with individual masses comparable to dwarf planets like Pluto (diameter  $\sim 2400$  km) or Varuna (diameter  $\sim 700$  km), and collective masses ranging from  $\sim 10$ – $10^3 m_{\oplus}$ . Having many stirrers opens the door to having a fraction of them collide over the system age. Indeed half of the disks in our sample have been argued to exhibit the scattered-light signatures of recent giant impacts: AU

Mic (Chiang & Fung 2017) and HD 15115 and HD 32297 (Jones et al. 2023). Taking these candidate giant impact systems as examples, we found that in certain regions of parameter space,  $\sim 20$ – $60\%$  of the stirring population can collide over system ages, releasing enough debris to contribute toward, and perhaps even source entirely, the collisional cascades generating the observable small bodies. In other words, the time-averaged rate at which Varuna to Pluto-sized stirrers collide and inject debris into the disk can in principle match the rate at which cascades grind mass down into observable  $\mu\text{m}$  to mm-sized dust. Future work can model how freshly injected debris from giant impacts relaxes into a quasi-steady cascade, distinguishing between the injection size spectrum (typically cited with a differential size index  $q = 4$  which distributes mass equally across mass bins; e.g. Gault et al. 1963; Takasawa et al. 2011; Leinhardt & Stewart 2012; Kral et al. 2015) and the collisionally relaxed spectrum ( $q = 3.5$ ; e.g. Dohnanyi 1969; Pan & Sari 2005; Wyatt et al. 2011).

To recap, it is unclear whether the big body stirrers are large (planet sized), few, and collisionless; or small (dwarf planet sized), many, and collisional. These possibilities are also not mutually exclusive. In addition to exploring origin scenarios for the big body stirrers, one can also try to divine their fate. Our self-stirring parameters imply that big body collisions are strongly gravitationally focussed and therefore largely accretionary — only a small fraction,  $f_{debris} \sim$  a few percent, of the colliding mass is ejected into interplanetary space (we assumed  $f_{debris} = 3\%$  in our cascade sourcing statements above).

The viscously stirring bodies in debris disks, if there are enough of them, may not be done growing.

Gas drag on particles damps inclinations and suppresses the formation of thick vertical tails, more so for smaller particles. Two disks out of our ARKS III subsample have CO gas detections, HD 32297 and HD 131488. For HD 32297 which exhibits a vertically Lorentzian profile at mm wavelengths, we hypothesize that despite its CO gas detection, there is insufficient total gas to drag the mm-sized grains presumed responsible for the ALMA emission out of their Lorentzian tails. Olofsson et al. (2022) showed that for gas masses  $\lesssim 0.1 m_{\oplus}$  — such modest masses may characterize gas that is collisionally generated (second-generation) — mm-sized grains can be relatively immune to gas drag (the same is not necessarily true for  $\mu\text{m}$ -sized grains, which could be dragged into a thin layer at the midplane). This interpretation is consistent with current estimates for the amount of gas in HD 32297, which overlap with  $\sim 0.1 m_{\oplus}$  (Cataldi et al. 2023, their Figures 8, 9, and 11).

### 5.2. *Alternative explanations of non-Gaussian vertical profiles*

Out-of-equipartition viscous stirring is not the only explanation for vertical density profiles having thick non-Gaussian tails. Having a dynamically “hot” population implanted by planetary migration on top of a “cold” population, as in the Kuiper belt, remains viable (Matrà et al. 2019). Degeneracies between vertical and radial structures are a perennial worry. Many of the ARKS III disks are radially extended, and line-of-sight projection of radial structures can mimic vertically extended structures. We found that even a vertically Gaussian disk with a constant vertical-to-horizontal aspect ratio (constant aspect ratios are the default assumption in ARKS fitting routines) can exhibit vertical density distributions with broad non-Gaussian tails, if such disks span more than a factor of a few in radius and are viewed edge-on (see also Olofsson et al. 2022). The ARKS III fitting procedure explicitly accounts for such 3D projection effects, and still finds evidence for non-Gaussian vertical profiles. Nevertheless vertical Gaussians with radially varying aspect ratios (e.g. Sefilian et al. 2025) could be lurking in the data.

Still another possibility is a particle size distribution where different sized particles have different scale heights to yield a non-Gaussian emissivity (Terrill et al. 2023, their Figure 14). More flexible methods available for mapping disk substructures are **frank** (Jennings et al. 2020; Terrill et al. 2023), and **rave** (Han et al.

2022, Han et al. 2025), which fit for radial structures non-parametrically. Current implementations of these algorithms assume vertical Gaussians, a restriction that could be relaxed for future work. Measuring how disk images vary with wavelength from the sub-mm through the radio, uncomplicated by the effects of radiation pressure (cf. Han et al. 2026a, Rebollido et al. 2024), can also help to sort between hypotheses (Vizgan et al. 2022).

We thank Yoram Lithwick, Miguel Martinez, and Tuhin Ghosh for discussions, and acknowledge the use of A.I. tools (Claude.ai, Gemini, ChatGPT) for assistance in coding, pointers to the literature, and conversation partners for exploring ideas. The authors take full responsibility for the content of this paper; no part of the text was generated by an A.I. EC is supported by the Simons Investigator program and the Miller Institute for Basic Research in Science, University of California, Berkeley. TDP is supported by a UKRI Stephen Hawking Fellowship and a Warwick Prize Fellowship, the latter made possible by a generous philanthropic donation. MRJ acknowledges funding provided by the Institute of Physics Belgrade, through the grant by the Ministry of Science, Technological Development, and Innovations of the Republic of Serbia. YH is supported by a Barr Fellowship at Caltech. Support for BZ was provided by The Brinson Foundation. AMH gratefully acknowledges support from the National Science Foundation under Grant No. AST-2307920. JBL acknowledges the Smithsonian Institution for funding via a CfA J.C. Ryan Fellowship. SM acknowledges funding by the Royal Society through a Royal Society University Research Fellowship (URF-R1-221669) and the European Union through the FEED ERC project (grant number 101162711). Views and opinions expressed are however those of the authors only and do not necessarily reflect those of the European Union or the European Research Council Executive Agency. Neither the European Union nor the granting authority can be held responsible for them. AAS is supported by the Heising-Simons Foundation through a 51 Pegasi b Fellowship. MW was supported by the Science and Technology Facilities Council grant UKRI1198. PA received funding from the Hungarian NKFIH project No. K-147380. AK is supported by the NKFIH NKKP grant ADVANCED 149943, which has been implemented with the support provided by the Ministry of Culture and Innovation of Hungary from the National Research, Development and Innovation Fund, financed under the NKKP ADVANCED funding scheme.

## REFERENCES

- Ahmic, M., Croll, B., & Artymowicz, P. 2009, *ApJ*, 705, 529, doi: [10.1088/0004-637X/705/1/529](https://doi.org/10.1088/0004-637X/705/1/529)
- Boccaletti, A., Thalmann, C., Lagrange, A.-M., et al. 2015, *Nature*, 526, 230, doi: [10.1038/nature15705](https://doi.org/10.1038/nature15705)
- Boccaletti, A., Sezestre, E., Lagrange, A.-M., et al. 2018, *A&A*, 614, A52, doi: [10.1051/0004-6361/201732462](https://doi.org/10.1051/0004-6361/201732462)
- Bouchaud, J.-P., & Georges, A. 1990, *PhR*, 195, 127, doi: [10.1016/0370-1573\(90\)90099-N](https://doi.org/10.1016/0370-1573(90)90099-N)
- Cataldi, G., Aikawa, Y., Iwasaki, K., et al. 2023, *ApJ*, 951, 111, doi: [10.3847/1538-4357/acd6f3](https://doi.org/10.3847/1538-4357/acd6f3)
- Chambers, J. E., Wetherill, G. W., & Boss, A. P. 1996, *Icarus*, 119, 261, doi: [10.1006/icar.1996.0019](https://doi.org/10.1006/icar.1996.0019)
- Chandrasekhar, S. 1943, *Reviews of Modern Physics*, 15, 1, doi: [10.1103/RevModPhys.15.1](https://doi.org/10.1103/RevModPhys.15.1)
- Chiang, E., & Fung, J. 2017, *ApJ*, 848, 4, doi: [10.3847/1538-4357/aa89e6](https://doi.org/10.3847/1538-4357/aa89e6)
- Collins, B. F., & Sari, R. 2006, *AJ*, 132, 1316, doi: [10.1086/506388](https://doi.org/10.1086/506388)
- Collins, B. F., Schlichting, H. E., & Sari, R. 2007, *AJ*, 133, 2389, doi: [10.1086/513718](https://doi.org/10.1086/513718)
- Daley, C., Hughes, A. M., Carter, E. S., et al. 2019, *ApJ*, 875, 87, doi: [10.3847/1538-4357/ab1074](https://doi.org/10.3847/1538-4357/ab1074)
- Dohnanyi, J. S. 1969, *J. Geophys. Res.*, 74, 2531, doi: [10.1029/JB074i010p02531](https://doi.org/10.1029/JB074i010p02531)
- Emsenhuber, A., Cambioni, S., Asphaug, E., et al. 2020, *ApJ*, 891, 6, doi: [10.3847/1538-4357/ab6de5](https://doi.org/10.3847/1538-4357/ab6de5)
- Feller, W. 1971, *An introduction to probability theory and its applications* (Wiley)
- Fernández-Valenzuela, E., Ortiz, J. L., Morales, N., et al. 2019, *ApJL*, 883, L21, doi: [10.3847/2041-8213/ab40c2](https://doi.org/10.3847/2041-8213/ab40c2)
- Frank, J., King, A., & Raine, D. J. 2002, *Accretion Power in Astrophysics: Third Edition* (Cambridge University Press)
- Gault, D. E., Shoemaker, E. M., & Moore, H. J. 1963, *Spray Ejected from the Lunar Surface by Meteoroid Impact*, Tech. Rep. D-1767, NASA
- Gladman, B. 1993, *Icarus*, 106, 247, doi: [10.1006/icar.1993.1169](https://doi.org/10.1006/icar.1993.1169)
- Goldreich, P., Lithwick, Y., & Sari, R. 2004, *ARA&A*, 42, 549, doi: [10.1146/annurev.astro.42.053102.134004](https://doi.org/10.1146/annurev.astro.42.053102.134004)
- Han, Y., Wyatt, M. C., Jankovic, M. R., et al. 2026a, arXiv e-prints, arXiv:2603.03540, doi: [10.48550/arXiv.2603.03540](https://doi.org/10.48550/arXiv.2603.03540)
- Han, Y., Wyatt, M. C., & Marino, S. 2025, *MNRAS*, 537, 3839, doi: [10.1093/mnras/staf282](https://doi.org/10.1093/mnras/staf282)
- Han, Y., Wyatt, M. C., & Matrà, L. 2022, *MNRAS*, 511, 4921, doi: [10.1093/mnras/stac373](https://doi.org/10.1093/mnras/stac373)
- Han, Y., Mansell, E., Jennings, J., et al. 2026b, *A&A*, 705, A196 (ARKS II), doi: [10.1051/0004-6361/202556450](https://doi.org/10.1051/0004-6361/202556450)
- Huang, Y., Gladman, B., Beaudoin, M., & Zhang, K. 2022, *ApJL*, 938, L23, doi: [10.3847/2041-8213/ac9480](https://doi.org/10.3847/2041-8213/ac9480)
- Ida, S., & Makino, J. 1992, *Icarus*, 96, 107, doi: [10.1016/0019-1035\(92\)90008-U](https://doi.org/10.1016/0019-1035(92)90008-U)
- . 1993, *Icarus*, 106, 210, doi: [10.1006/icar.1993.1167](https://doi.org/10.1006/icar.1993.1167)
- Jankovic, M. R., Wyatt, M. C., & Löhne, T. 2024, *A&A*, 691, A302, doi: [10.1051/0004-6361/202451080](https://doi.org/10.1051/0004-6361/202451080)
- Jennings, J., Booth, R. A., Tazzari, M., Rosotti, G. P., & Clarke, C. J. 2020, *MNRAS*, 495, 3209, doi: [10.1093/mnras/staa1365](https://doi.org/10.1093/mnras/staa1365)
- Jones, J. W., Chiang, E., Duchêne, G., Kalas, P., & Esposito, T. M. 2023, *ApJ*, 948, 102, doi: [10.3847/1538-4357/acc466](https://doi.org/10.3847/1538-4357/acc466)
- Kalas, P., Graham, J. R., & Clampin, M. 2005, *Nature*, 435, 1067, doi: [10.1038/nature03601](https://doi.org/10.1038/nature03601)
- Kral, Q., Thébault, P., Augereau, J.-C., Boccaletti, A., & Charnoz, S. 2015, *A&A*, 573, A39, doi: [10.1051/0004-6361/201424309](https://doi.org/10.1051/0004-6361/201424309)
- Krivov, A. V., & Wyatt, M. C. 2021, *MNRAS*, 500, 718, doi: [10.1093/mnras/staa2385](https://doi.org/10.1093/mnras/staa2385)
- Leinhardt, Z. M., & Stewart, S. T. 2012, *ApJ*, 745, 79, doi: [10.1088/0004-637X/745/1/79](https://doi.org/10.1088/0004-637X/745/1/79)
- Lissauer, J. J., & Stewart, G. R. 1993, in *Protostars and Planets III*, ed. E. H. Levy & J. I. Lunine, 1061
- Lovell, J. B., Lynch, E. M., Chittidi, J., et al. 2025, *ApJ*, 990, 145, doi: [10.3847/1538-4357/adfadc](https://doi.org/10.3847/1538-4357/adfadc)
- Lovell, J. B., Hales, A. S., Kennedy, G. M., et al. 2026, *A&A*, 705, A200 (ARKS VI), doi: [10.1051/0004-6361/202556568](https://doi.org/10.1051/0004-6361/202556568)
- MacGregor, M. A., Matrà, L., Kalas, P., et al. 2017, *ApJ*, 842, 8, doi: [10.3847/1538-4357/aa71ae](https://doi.org/10.3847/1538-4357/aa71ae)
- Marino, S., Matrà, L., Hughes, A. M., et al. 2026, *A&A*, 705, A195 (ARKS I), doi: [10.1051/0004-6361/202556489](https://doi.org/10.1051/0004-6361/202556489)
- Matrà, L., Wyatt, M. C., Wilner, D. J., et al. 2019, *AJ*, 157, 135, doi: [10.3847/1538-3881/ab06c0](https://doi.org/10.3847/1538-3881/ab06c0)
- Murray, C. D., & Dermott, S. F. 1999, *Solar System Dynamics* (Cambridge University Press), doi: [10.1017/CBO9781139174817](https://doi.org/10.1017/CBO9781139174817)
- Nesvorný, D. 2018, *ARA&A*, 56, 137, doi: [10.1146/annurev-astro-081817-052028](https://doi.org/10.1146/annurev-astro-081817-052028)
- Olofsson, J., Thébault, P., Kral, Q., et al. 2022, *MNRAS*, 513, 713, doi: [10.1093/mnras/stac455](https://doi.org/10.1093/mnras/stac455)
- Pan, M., & Sari, R. 2005, *Icarus*, 173, 342, doi: [10.1016/j.icarus.2004.09.004](https://doi.org/10.1016/j.icarus.2004.09.004)
- Pearce, T. D., Löhne, T., & Krivov, A. V. 2025, *MNRAS*, 544, 1447, doi: [10.1093/mnras/staf1735](https://doi.org/10.1093/mnras/staf1735)
- Pearce, T. D., Krivov, A. V., Sefilian, A. A., et al. 2024, *MNRAS*, 527, 3876, doi: [10.1093/mnras/stad3462](https://doi.org/10.1093/mnras/stad3462)
- Rebollido, I., Stark, C. C., Kammerer, J., et al. 2024, *AJ*, 167, 69, doi: [10.3847/1538-3881/ad1759](https://doi.org/10.3847/1538-3881/ad1759)
- Rein, H., & Liu, S.-F. 2012, *A&A*, 537, A128, doi: [10.1051/0004-6361/201118085](https://doi.org/10.1051/0004-6361/201118085)

- Rein, H., Hernandez, D. M., Tamayo, D., et al. 2019, MNRAS, 485, 5490, doi: [10.1093/mnras/stz769](https://doi.org/10.1093/mnras/stz769)
- Rybicki, G. B., & Lightman, A. P. 1986, Radiative Processes in Astrophysics (Wiley)
- Sefilian, A. A., Kratter, K. M., Wyatt, M. C., et al. 2025, MNRAS, 543, 3123, doi: [10.1093/mnras/staf1555](https://doi.org/10.1093/mnras/staf1555)
- Strubbe, L. E., & Chiang, E. I. 2006, ApJ, 648, 652, doi: [10.1086/505736](https://doi.org/10.1086/505736)
- Takasawa, S., Nakamura, A. M., Kadono, T., et al. 2011, ApJL, 733, L39, doi: [10.1088/2041-8205/733/2/L39](https://doi.org/10.1088/2041-8205/733/2/L39)
- Tamayo, D., Rein, H., Shi, P., & Hernandez, D. M. 2020, MNRAS, 491, 2885, doi: [10.1093/mnras/stz2870](https://doi.org/10.1093/mnras/stz2870)
- Terrill, J., Marino, S., Booth, R. A., et al. 2023, MNRAS, 524, 1229, doi: [10.1093/mnras/stad1847](https://doi.org/10.1093/mnras/stad1847)
- Vizgan, D., Hughes, A. M., Carter, E. S., et al. 2022, ApJ, 935, 131, doi: [10.3847/1538-4357/ac80b8](https://doi.org/10.3847/1538-4357/ac80b8)
- Wisdom, J. 1980, AJ, 85, 1122, doi: [10.1086/112778](https://doi.org/10.1086/112778)
- Wyatt, M. C., Clarke, C. J., & Booth, M. 2011, Celestial Mechanics and Dynamical Astronomy, 111, 1, doi: [10.1007/s10569-011-9345-3](https://doi.org/10.1007/s10569-011-9345-3)
- Zawadzki, B., Fehr, A., Hughes, A. M., et al. 2026, A&A, 705, A197 (ARKS III), doi: [10.1051/0004-6361/202556505](https://doi.org/10.1051/0004-6361/202556505)

## APPENDIX

In Appendix A we show how viscous stirring in shear-dominated disks leads to vertical Lorentzians. Appendix B contains some results from our single big body numerical integrations. These  $N$ -body runs support our findings of vertical Lorentzians while also exhibiting a few artifacts resulting from our assumption of a single big body. In Appendix C we derive how small body eccentricities  $e$  and inclinations  $i$  grow with time when the perturbing big bodies have eccentricities  $e_b > e$ , and how our results in Figs. 14 and 15 may change as a consequence.

## A. VERTICAL SCATTERING IN SHEAR-DOMINATED PARTICLE DISKS

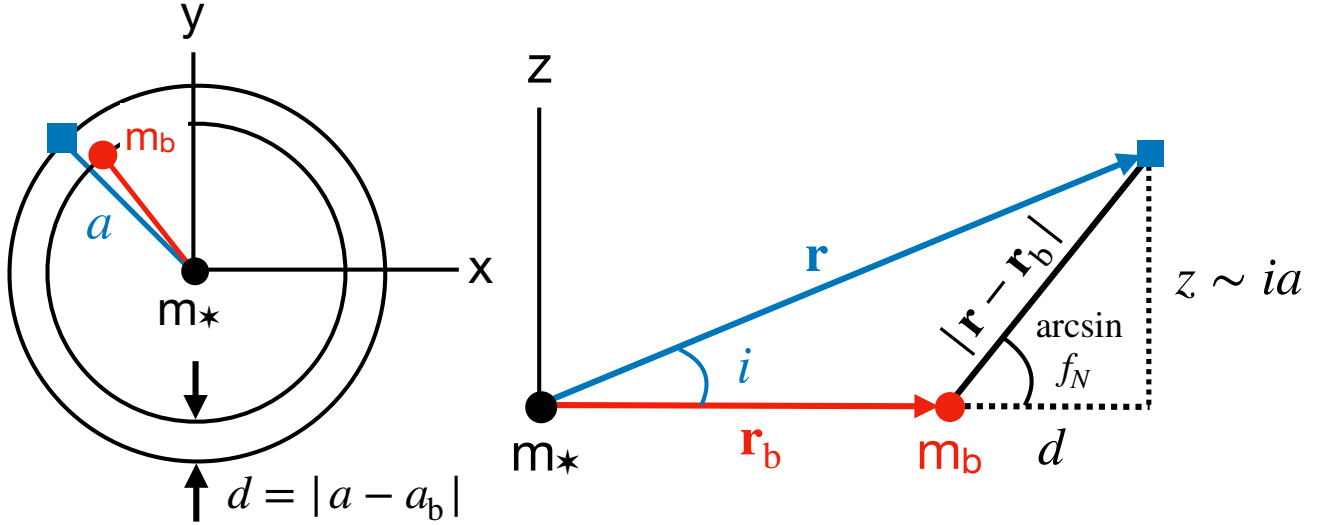


**Figure 16.** Same as Figure 4, but now for a shear-dominated configuration between a big body of mass  $m_b$  (red circle) and a small body (test particle, blue square), both on circular orbits separated in semimajor axis by  $d = |a - a_b|$ . The bodies have similar semimajor axes  $a \gg d$ . At the moment of encounter (conjunction), the small body feels a vertical gravitational acceleration which is less than the full gravitational acceleration by a factor of  $|f_N|$ , by definition. To order of magnitude,  $|f_N| \sim ia/d$ .

We show that the same  $|\Delta i| \propto i$  scaling for scatterings in a dispersion-dominated, out-of-equipartition disk holds in a shear-dominated disk, where bodies are not on crossing orbits and their relative velocities are controlled by the background Keplerian shear instead of by eccentricities and inclinations. Figure 16 shows the setup: a small body (test particle) and a big body perturber of mass  $m_b$ , separated in semimajor axis by  $d \equiv |a_b - a| \ll a$ . We measure  $d \equiv FR_H$  in units of the big body's Hill radius  $R_H = [m_b/(3m_*)]^{1/3}a_b = (\mu_b/3)^{1/3}a_b$  with  $F > 1$ , and define a Hill eccentricity and inclination,  $e_H = i_H \equiv (\mu_b/3)^{1/3}$ .

The relative shearing velocity between the bodies is  $v_{\text{rel}} \simeq (3/2)nd$ , where  $n$  is the local mean motion. Under the same impulse approximation that we used to write down eqs. (5) and (6), every close encounter (conjunction) changes the small body eccentricity by:

$$\Delta e \sim \pm \frac{1}{v_K} \cdot \frac{Gm_b}{d^2} \cdot \frac{2d}{v_{\text{rel}}} \sim \pm \frac{4}{F^2} e_H. \quad (\text{A1})$$

The inclination change is derived the same way except that it is downweighted by the factor  $f_N$ , whose magnitude is of order  $ia$  (vertical epicyclic excursion) divided by  $d$  (horizontal separation; see Fig. 16):

$$\Delta i \sim \pm \Delta e \cdot f_N \sim \pm \frac{4}{F^3} i \quad (\text{A2})$$



valid for  $ia < d$  or equivalently  $i < Fi_H$  (sub-Hill inclinations). Thus  $\Delta i \propto i$ , and repeated encounters (assuming they are uncorrelated; for a single big body this requires  $F \lesssim 3$  for the small body to stay within the big body’s chaotic zone) should lead to diffusion in  $\log i$  and by extension a vertical Lorentzian profile. Eccentricities should grow faster than inclinations insofar as  $\Delta e > \Delta i$ , as appears borne out at early times for our  $N$ -body Runs E and EE (Table 1). We could go further to explore shear-dominated stirring rates (e.g. *Ida & Makino 1993; Goldreich et al. 2004*), but are unmotivated to do so as *Jankovic et al. (2026)* have shown that debris disks could not have been stirred to their present states under shear-dominated conditions.

## B. NUMERICAL INTEGRATIONS WITH A SINGLE BIG BODY

Figures 17–19 document Run A, whose results parallel those of Run BB (Figs. 8–10; see Table 1 for parameters, and captions for details). Note how in Fig. 19 the test particle disk is becoming globally eccentric, conforming to the eccentric orbit of the big body. This is a consequence of our using only a single eccentric big body in Run A to perturb the small bodies (if there were instead many big bodies on crossing orbits with randomly oriented apsides, the small bodies would be perturbed into an axisymmetric disk).

In the other single big body runs C, D, and E, test particle inclinations are anti-correlated with eccentricities (data not shown). This follows from the Jacobi constant being conserved when there is only a single big body with  $e_b = 0$  (*Murray & Dermott 1999*). Such an anti-correlation is not present in our other runs where small bodies are stirred by eccentric or multiple big bodies. The anti-correlation does not affect the main finding of all our numerical integrations, that vertical Lorentzians manifest when  $e, e_b \gg 2i$ , and vertical Gaussians when  $e, e_b \simeq 2i$ .

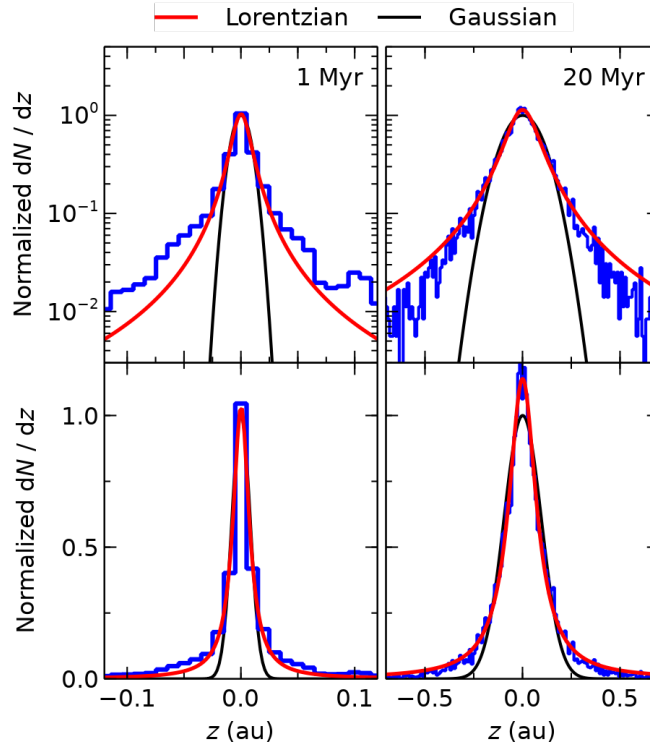


**Figure 17.** Vertical density profiles of test particles (a.k.a. small bodies) simulated with REBOUND in Run A at  $t = 1$  Myr (left panel) and 20 Myr (right). Run A features a single big body with a large eccentricity ( $e_b = 0.1$ ) and small initial mutual inclination with test particles ( $10^{-5}$  rad); for most of the evolution, in-plane relative velocities between the big body and small bodies will exceed out-of-plane relative velocities. We expect under such circumstances that small bodies take inclination steps  $\Delta i \propto \pm i$  (Section 2) and that their vertical distributions (blue histograms) resemble Lorentzians (red curves) more than Gaussians (black curves). Test particles having  $i < 10^{-4}$  (constituting 55% of all test particles at  $t = 1$  Myr, and 0.15% at 20 Myr) have been omitted as these reflect too strongly our assumed initial inclinations of  $10^{-5}$  rad). The horizontal axis changes scale by a factor of 5 between left and right columns as the disk thickens vertically with time.

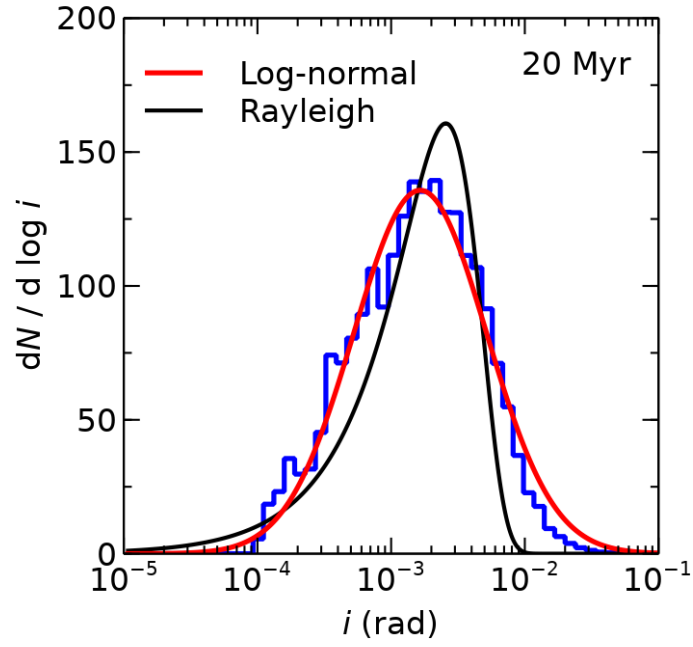


**Figure 18.** Inclination distribution of test particles for Run A (single big body with  $e_b = 0.1$ , test particles on initially circular orbits) at  $t = 20$  Myr (blue histogram, unnormalized). Overlaid are a best-fit log normal distribution (red curve) and a Rayleigh distribution (black curve). The log normal fits better, as expected when in-plane relative velocities between the big body and test particles greatly exceed out-of-plane relative velocities, and small bodies random walk with fixed steps in  $\Delta \ln i$  (Section 2).

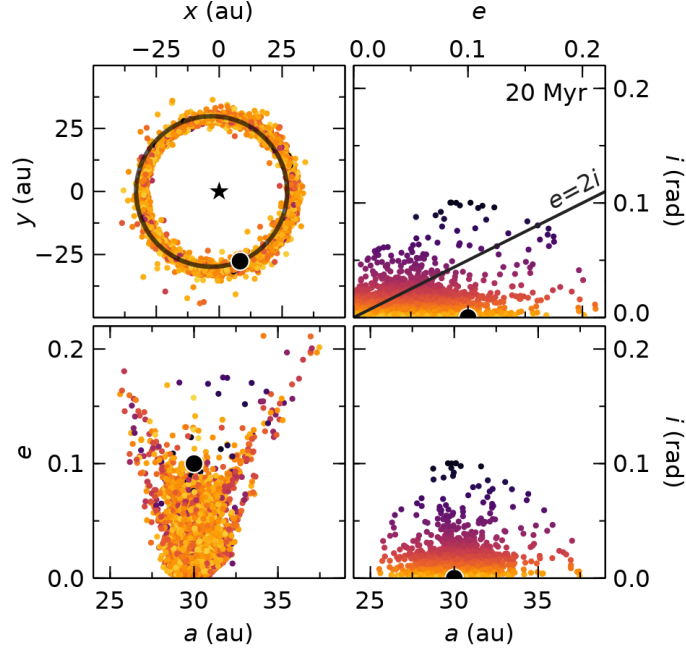


**Figure 19.** Orbital elements for Run A (single big body with  $e_b = 0.1$ , test particles on initially circular orbits) at  $t = 20$  Myr. In all panels, test particles are represented by colored points, and the big body is represented by a black disc. *Top left:* Snapshot of test particles, the big body and its orbit, and the host star in the  $x$ - $y$  plane. Note how the test particles have been sculpted into a globally eccentric disk, apsidally aligned with the single eccentric big body. *Top right:* Inclinations  $i$  vs. eccentricities  $e$  for the big body and test particles. The test particle points are colored according to their inclinations; the same color scheme is used for all panels. The  $e = 2i$  line represents equipartition between in-plane and out-of-plane motions; most bodies have  $i < e/2$ , a requirement for  $|\Delta i| \propto i$  (Section 2). *Bottom left:* Eccentricities  $e$  vs. semimajor axes  $a$ . *Bottom right:* Inclinations  $i$  vs. semimajor axes  $a$ .

### C. VISCOUS STIRRING WHEN BIG BODY ECCENTRICITIES $>$ SMALL BODY ECCENTRICITIES

In Section 2.5 we worked out how mutual inclinations  $i$  and small body eccentricities  $e$  evolved with time when big body eccentricities  $e_b \lesssim e$ . In that case we could ignore  $e_b$  compared to  $e$  when estimating the relative velocities between small and big bodies. Here we examine the converse case  $e_b > e$  and solve for  $e(t)$  and  $i(t)$ , under the simplifying assumption that  $e_b$  is fixed. Replacing  $e$  with  $e_b$  in eqs. (5) and (6), we see that eqs. (8) and (9) for the inclination and eccentricity doubling times become modified to depend on  $e_b$ :

$$t_{\text{double } i} \equiv \frac{i}{di/dt} \sim \left( \frac{i}{\Delta i} \right)^2 t_{b\parallel} \sim \frac{e_b^4}{A_i^2} \frac{m_\star}{\Sigma_b a^2} \frac{1}{\mu_b} \frac{1}{n} \quad (\text{C3})$$

$$t_{\text{double } e} \equiv \frac{e}{de/dt} \sim \left( \frac{e}{\Delta e} \right)^2 t_{b\parallel} \sim \frac{e_b^4}{A_e^2} \frac{m_\star}{\Sigma_b a^2} \frac{1}{\mu_b} \frac{1}{n}. \quad (\text{C4})$$

As the right-hand sides of these equations are now constants,  $i$  and  $e$  grow exponentially with time:

$$i = i_0 \exp(t/T_i) \quad (\text{C5})$$

$$e = e_0 \exp(t/T_e) \quad (\text{C6})$$

with time constants

$$T_i = \frac{e_b^4}{A_i^2} \frac{m_\star}{\Sigma_b a^2} \frac{1}{\mu_b} \frac{1}{n} \quad (\text{C7})$$

$$T_e = \frac{e_b^4}{A_e^2} \frac{m_\star}{\Sigma_b a^2} \frac{1}{\mu_b} \frac{1}{n}. \quad (\text{C8})$$

As usual in the dispersion-dominated regime, inclination grows faster than eccentricity ( $T_e/T_i = A_i^2/A_e^2 \simeq 8$ , modulo the caveat that we have neglected Coulomb logs and other order-unity constants).

Following the same reasoning that led to equation (14) which jointly constrained  $\Sigma_b$  and  $\mu_b$  for a given present-day  $e \lesssim e_b$ , we solve for  $t = t_{\text{age}}$  in equation (C8):

$$t_{\text{age}} \sim \frac{e_b^4}{A_e^2} \frac{m_\star}{\Sigma_b a^2} \frac{1}{\mu_b} \frac{1}{n} \ln(e/e_0). \quad (\text{C9})$$

To within order-unity factors, equation (C9) for  $e_b > e$  presents a similar joint constraint on  $\Sigma_b$  and  $\mu_b$  as (14) does for  $e_b < e$ , the biggest difference being the replacement of the small body eccentricity  $e$  with the big body eccentricity  $e_b$ . Using eq. (C9) instead of eq. (14) would shift the allowed regions for debris disks in Figures 14 and 15 upward and to the right. Specifically the loci of possible  $\max m_b = \min M_{b,\text{tot}}$  would slide upward along the dashed line in Figs. 14 and 15 by a factor of  $[4 \ln(e/e_0)^{1/2} (e_b/e)^4]^{1/2} > 1$ , potentially an order of magnitude.

The above analysis assumes  $e_b$  is fixed. The big bodies will stir themselves, with eccentricities  $e_b$  and mutual inclinations  $i_b$  growing in power-law fashion according to eqs. (10)–(12) with  $e$ ,  $e_0$ ,  $i$ , and  $i_0$  replaced by their big body counterparts  $e_b$ ,  $e_{b,0}$ ,  $i_b$ , and  $i_{b,0}$ . As the big bodies stir each other algebraically slowly and stir the small bodies exponentially quickly, the small body eccentricities and inclinations eventually catch up to those of the big bodies, and the entire ensemble grows in tandem thereafter according to the self-stirring relations of Section 2.5.